Table of Content

A. Extended Figures

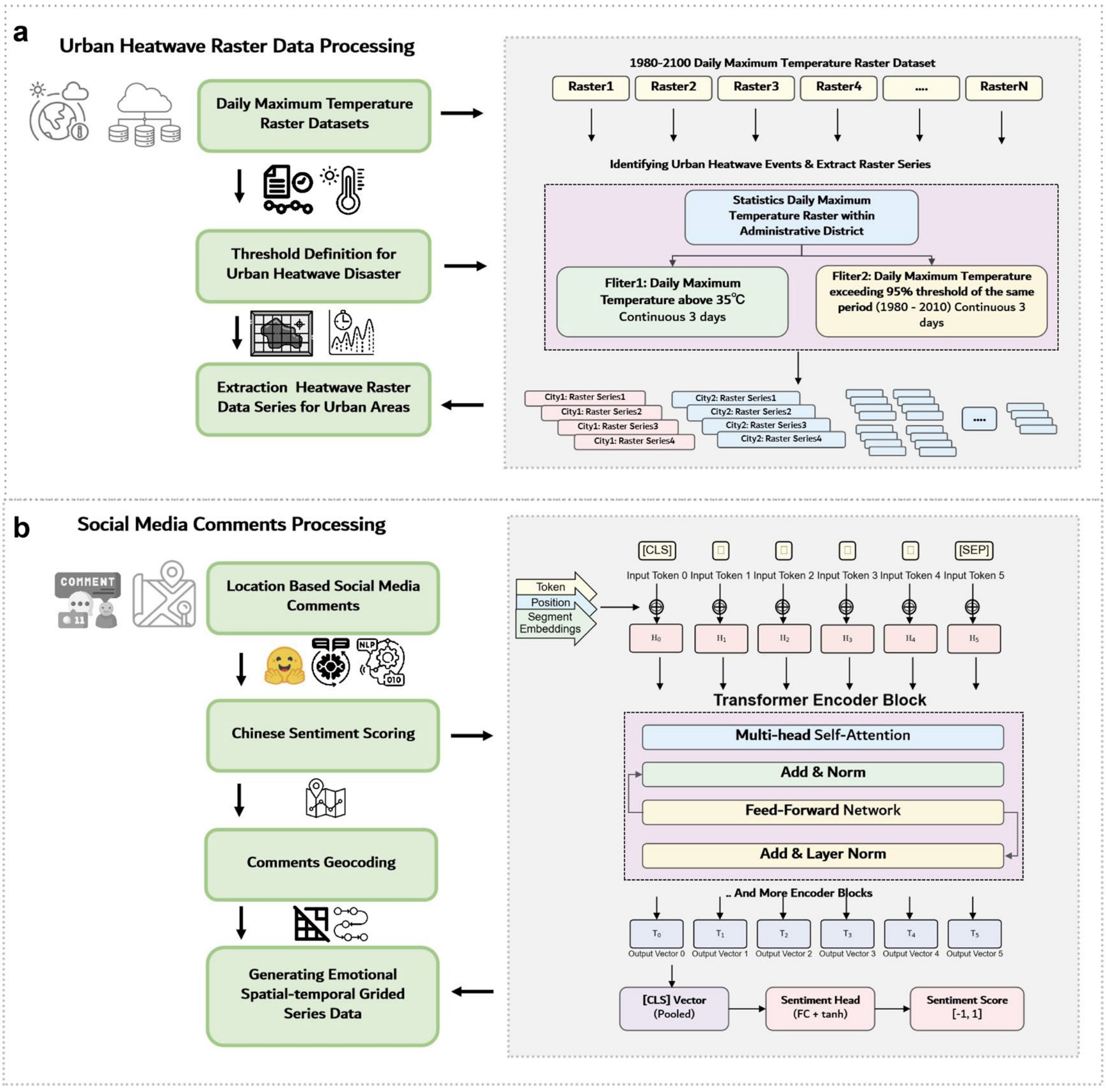

Extended Fig. 1. Data processing framework for identifying urban heatwave events and quantifying public sentiment.

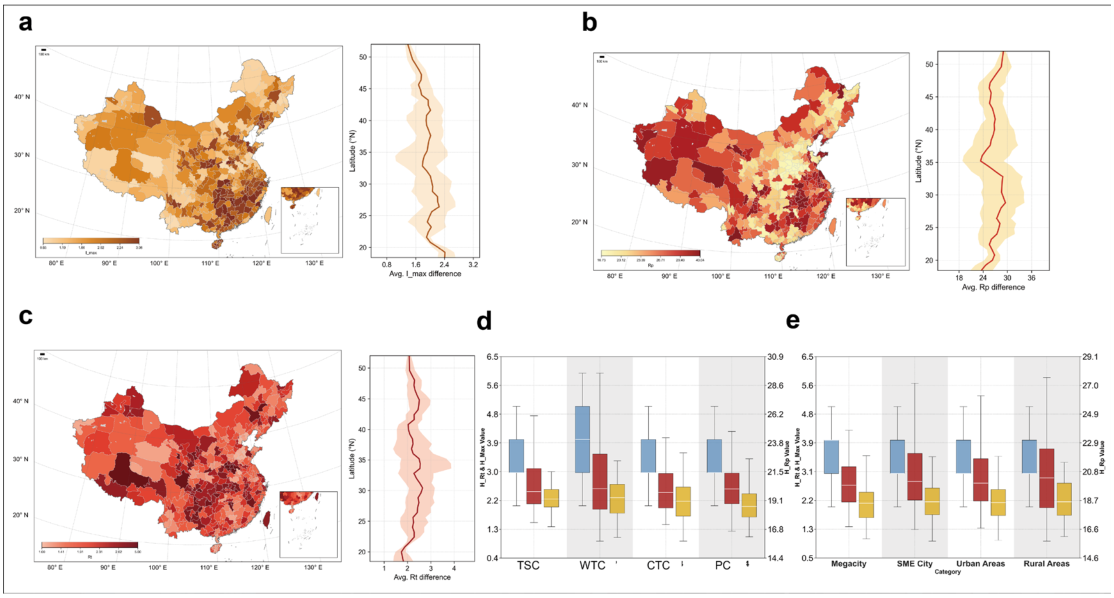

Extended Fig. 2. Spatial heterogeneity and statistical characteristics of urban heatwave attributes across China. a–c, Spatial distribution of $IMAX_h$; RP_h, and RT_h. The vertical plots to the right of each map display the latitudinal zonal means (solid lines) with shaded areas representing the standard deviation. d, Statistical distribution of heat metrics categorized by degree of urbanization: megacity cores, SME city, other urban areas, and rural areas. e, Statistical distribution categorized by climatic regions: TSC, WTC, CTC, and PC.

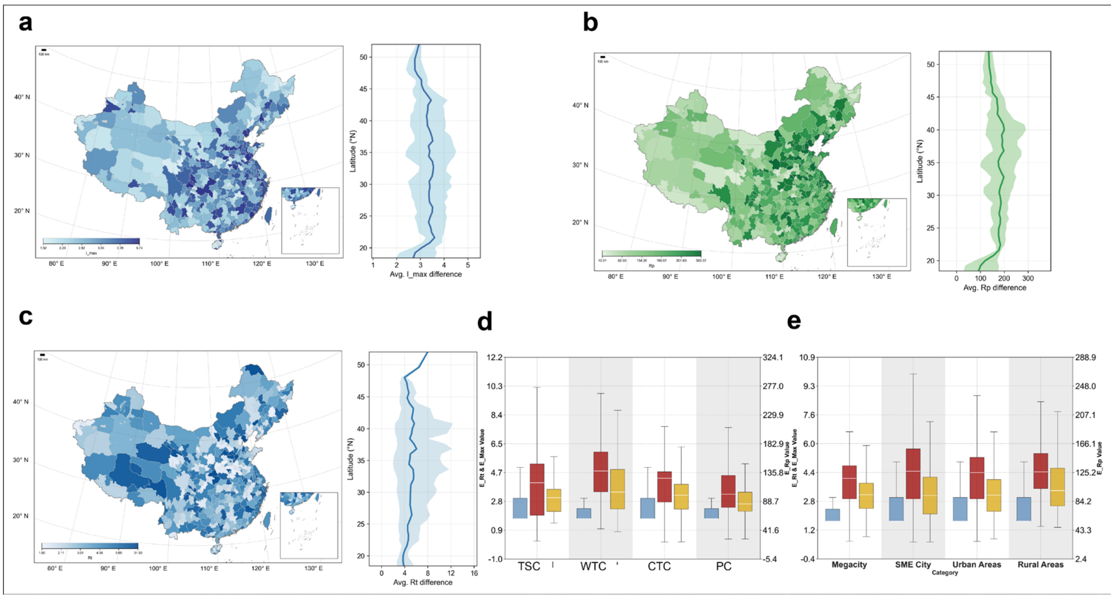

Extended Fig. 3. Spatial heterogeneity and statistical characteristics of emotion attributes across China. a–c, Spatial distribution of $IMAX_e$; RP_e, and RT_e. The vertical plots to the right of each map display the latitudinal zonal means (solid lines) with shaded areas representing the standard deviation. d, Statistical distribution of heat metrics categorized by degree of urbanization: megacity cores, SME city, other urban areas, and rural areas. e, Statistical distribution categorized by climatic regions: TSC, WTC, CTC, and PC.

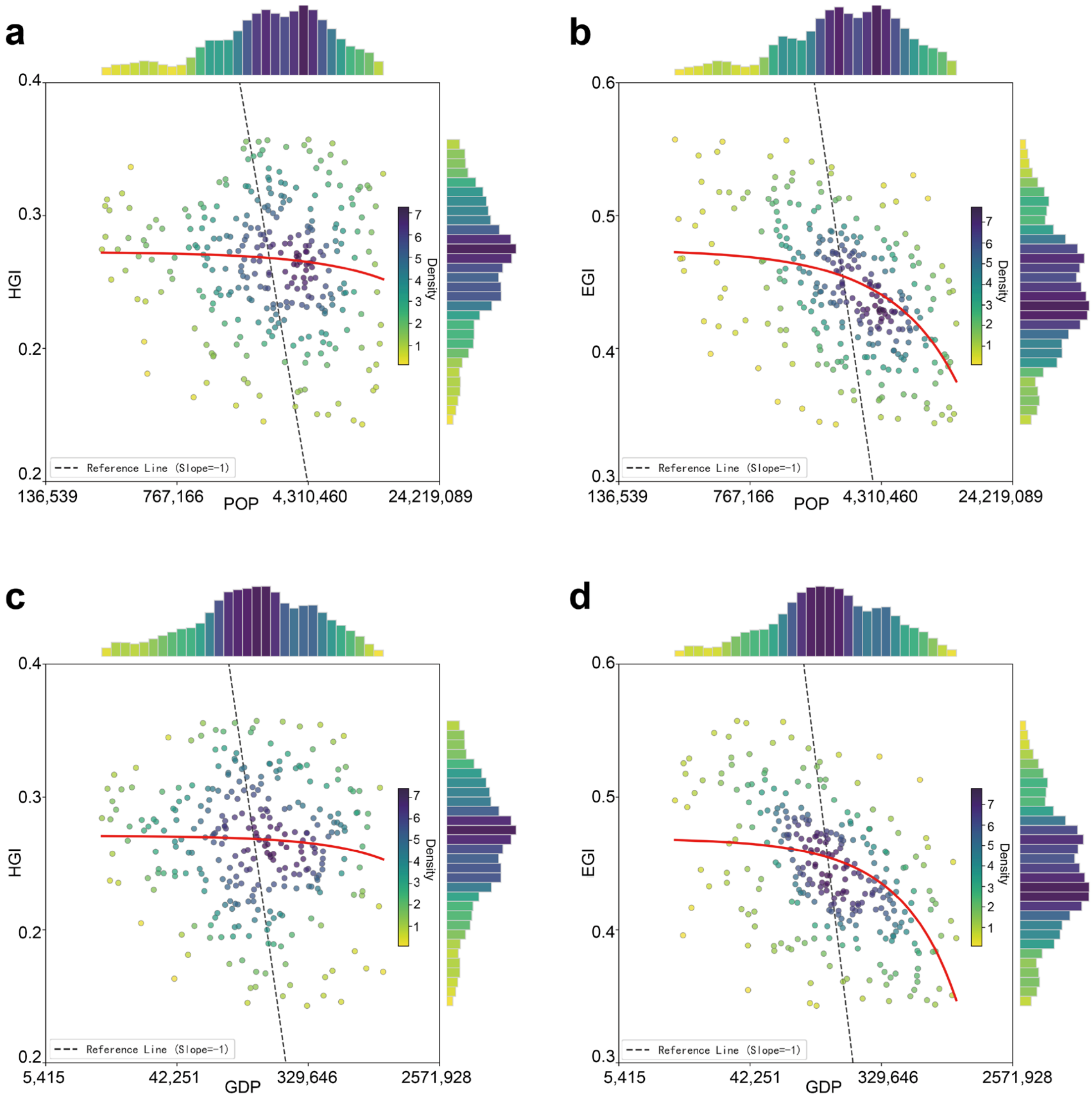

Extended Fig. 4. Scaling relationships of heat and emotional indices with socioeconomic determinants. Joint density plots of HGI (a, b) and EGI (c, d) against GDP and population. All axes are log-scaled. Colour gradients represent kernel density estimation (KDE), red curves show LOESS regression trends, and dashed lines indicate a reference slope of -1. Marginal histograms display univariate distributions.

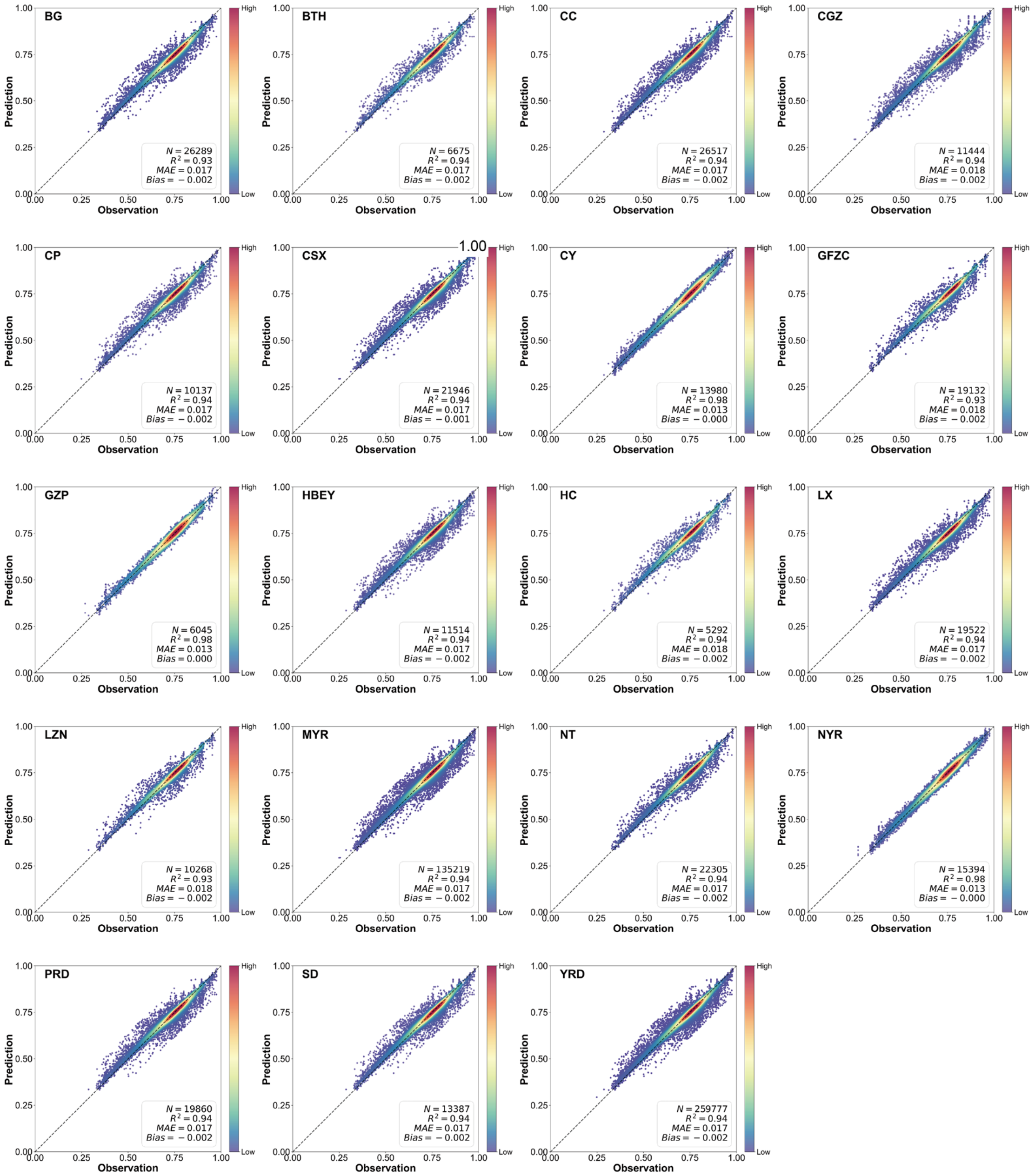

Extended Fig. 5. Performance evaluation of the LightGBM model across 19 city clusters.

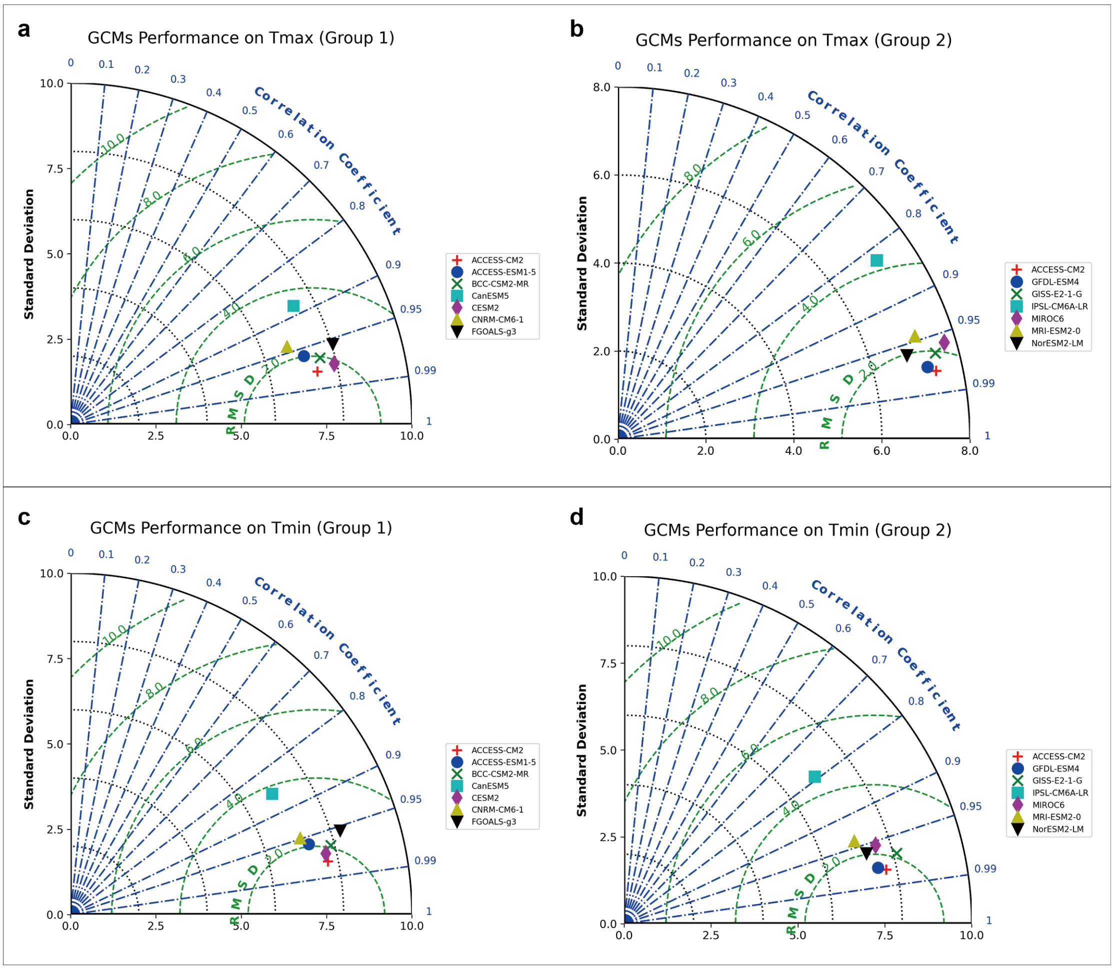

Extended Fig. 6. Taylor diagrams evaluating the performance of 13 CMIP6 global climate models. The diagrams assess model fidelity in simulating daily maximum temperature (T_{max}; a, b) and minimum temperature (T_{min}; c, d). Models are divided into two groups for visual clarity. In each plot, the azimuthal angle represents the correlation coefficient (CC), the radial distance indicates the standard deviation (SD), and the green dashed contours denote the centred root-mean-square difference (RMSD).

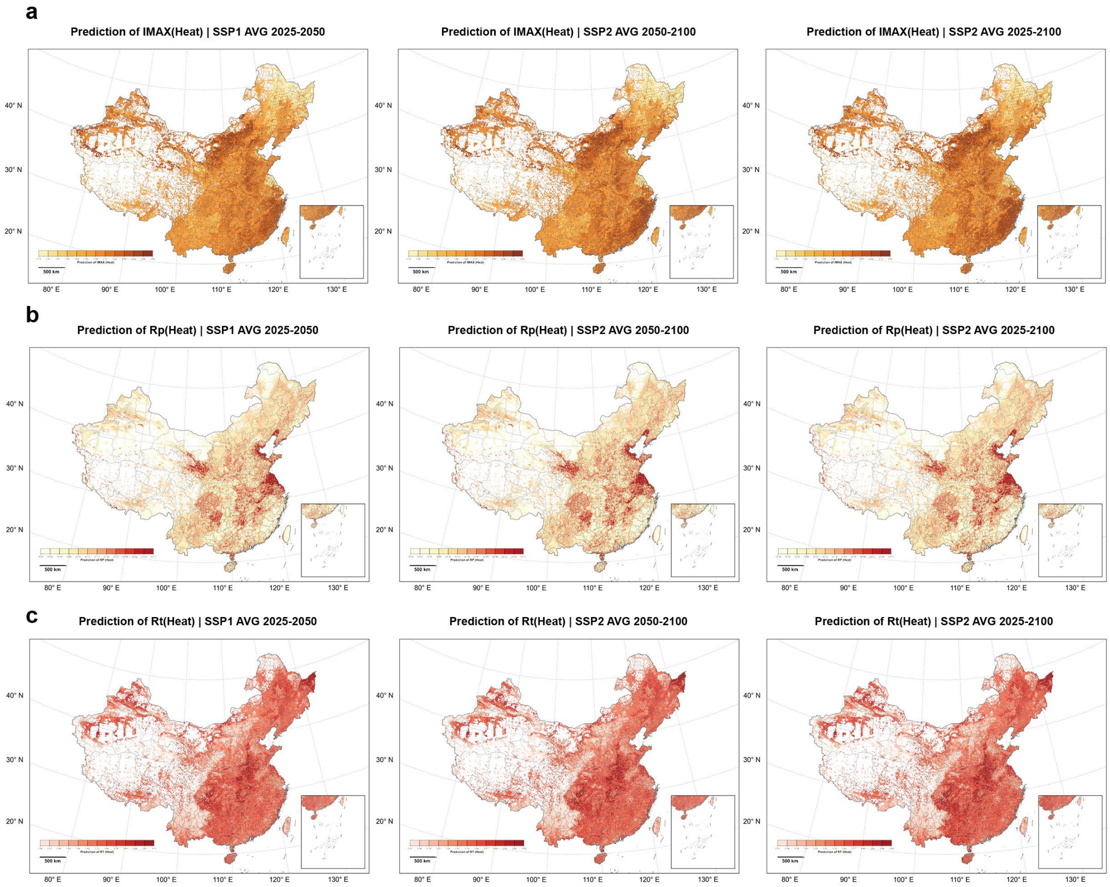

Extended Fig. 7. Future projections of decomposed HGI metrics under climate change scenarios. Maps illustrate the spatial distribution of the 75-year mean values (2025 – 2100) for Heat Peak Severity ($IMAX_h$; a), Heat Cumulative Perturbation Magnitude (RP_h; b), and Heat Recovery Time (RT_h; c). Columns correspond to SSP1-2.6 (left), SSP2-4.5 (middle), and SSP5-8.5 (right) scenarios.

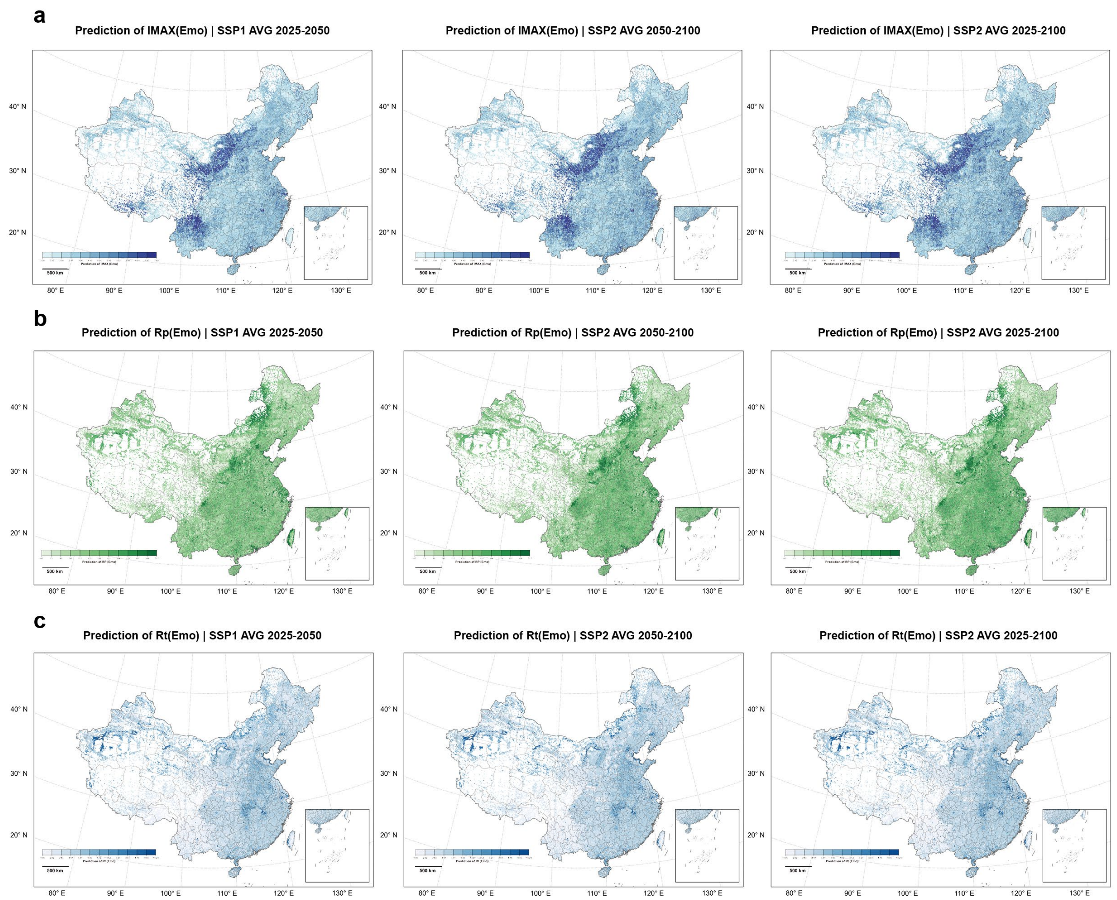

Extended Fig. 8. Future projections of decomposed EGI metrics under climate change scenarios. Maps illustrate the spatial distribution of the 75-year mean values (2025 – 2100) for Emotion Peak Severity ($IMAX_e$; a – c), Emotion Cumulative Perturbation Magnitude (RP_e; d – f), and Emotion Recovery Time (RT_e; g – i). Columns correspond to SSP1-2.6 (left), SSP2-4.5 (middle), and SSP5-8.5 (right) scenarios.

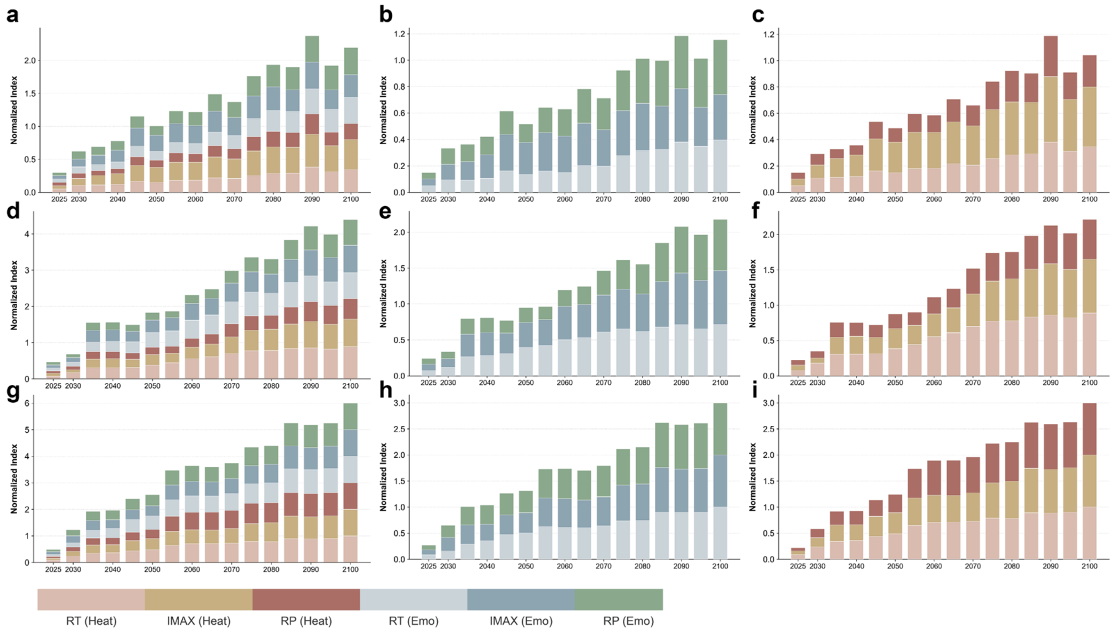

Extended Fig. 9. Projections of normalized resilience indices across climate scenarios (2025 – 2100). Plots display the stacked evolution of resilience components under SSP1-2.6 (a – c), SSP2-4.5 (d – f), and SSP5-8.5 (g – i). Panels represent the specific contributions of heat metrics (b, e, h: $IMAX_h$; RP_h, and RT_h) and emotion metrics (c, f, i: $IMAX_e$; RP_e, and RT_e), while a, d, and h show the comprehensive aggregation of all six indicators. The y-axis represents the normalized index value.

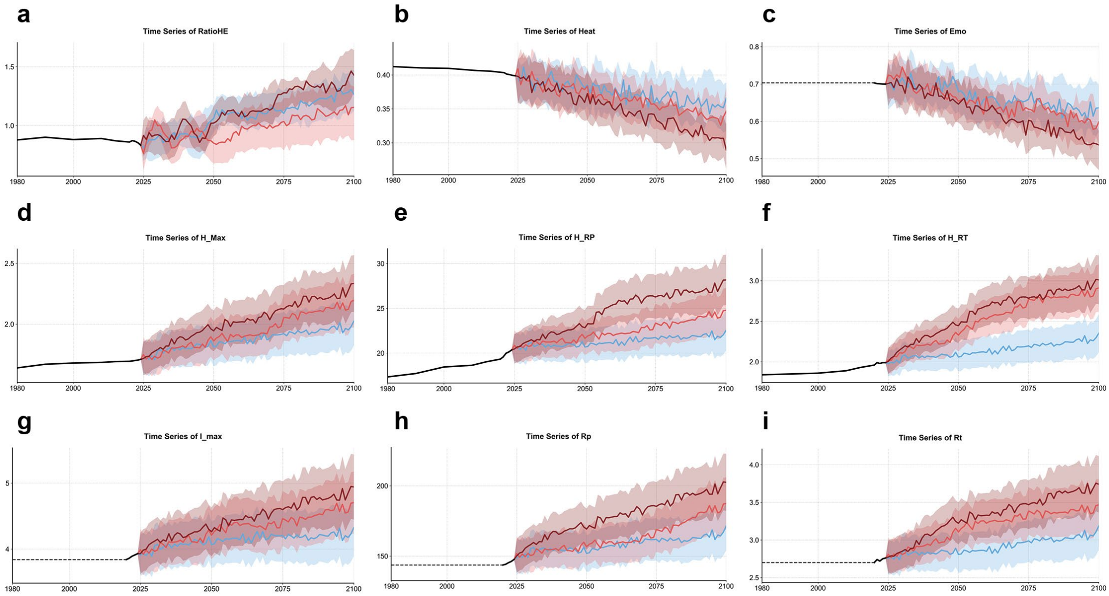

Extended Fig. 10. Divergent temporal trajectories of resilience metrics under climate change. Time series reconstructions (1980 – 2100) derived from 13 CMIP6 models. a, R_HE. b, c, HGI (b) and EGI (c). d – f, $IMAX_h$; RP_h, and RT_h (f). g – i, $IMAX_e$; RP_e, and RT_e. Black lines denote historical baselines (1980 – 2014); coloured lines represent SSP1-2.6 (blue), SSP2-4.5 (green) and SSP5-8.5 (red); shaded areas indicate 95% uncertainty bandwidths.

B. <u>Supplementary Notes</u>

Note S1: Socio-economic stratification and spatial inequity of urban heat resilience

The Lorenz curves and Gini coefficients collectively reveal that the distribution of resilience components is consistent yet diagnostically distinct across economic, demographic, and spatial weighting contexts (Supplementary Fig. 4). Under GDP weighting, the Emotional Recovery Time (RT_e) exhibits the strongest inequality (Gini = 0.64). Its curve remains significantly below the line of equality for most of the range before rising steeply at the tail, suggesting that a minority of high-GDP units contribute a disproportionate share of the *RTe* burden. In contrast, shock and cumulative load indicators show moderate concentration ($IMAX_e$ = 0.31, RP_e = 0.29), whereas physical metrics like RT_h (0.22) and $IMAX_h$ (0.20) are less concentrated. Notably, the concentration of aggregated indices is significantly compressed by the "aggregation effect," with HGI at 0.12 and EGI recording the lowest value (0.09). This proximity to the line of equality implies that composite emotional resilience is distributed nearly broadly in economic terms.

Weighting by population maintains the overall ranking, indicating that concentration is not driven solely by economic scale. RT_e remains the highest (0.63), confirming its high concentration even within the context of social equity. While $IMAX_e$ (0.31) and RP_e (0.27) maintain moderate deviation, RT_h rises to 0.24, suggesting a stronger demographic clustering of recovery rhythms. Meanwhile, RP_h drops to 0.11, and the composite indices remain low (HGI = 0.13, EGI = 0.08), indicating that inequality in comprehensive resilience diminishes significantly under demographic weighting. When weighted by area, spatial agglomeration features become more explicit. Although RT_e dips slightly, it remains high (0.59). The most critical shift occurs in shock intensity ($IMAX_e$), which rises to 0.37—surpassing its levels under GDP and population weighting (~0.31)—pointing to a distinct "spatially clustered" risk profile for extreme shocks. RP_e (0.29) and RT_h (0.26) also show slight increases. Conversely, RP_h is lowest under area weighting (0.09), indicating the weakest spatial clustering. Overall, the three weighting schemes confirm a robust conclusion: RT_e is consistently the most unequal component (0.59–0.64), EGI is consistently the most equal (0.08–0.09), whereas $IMAX_e$ is most sensitive to spatial weighting, reflecting its stronger geographic agglomeration.

The Local Disparity Index (LDI) results reveal that local inequality is characterized by distinct regional differentiation and transitional zones (Supplementary Fig. 3). In the physical dimension, high values of $IMAX_h$ tend to form patchy hotspots in the arid Northwest and inland basins, with local abrupt changes appearing at several eastern coastal endpoints, manifesting as a "shock intensity fracture" relative to surrounding units. By contrast, medium-to-high values of RT_h are more commonly distributed in bands or sheets across the Southwest mountain-basin transition zone, extending toward the Central-North China climatic transition belt. This suggests that recovery rhythm differences unfold continuously along regional gradients rather than being driven by isolated cities. RP_h is generally more fragmented with fewer high values, indicating weaker local disparity. At the composite level, the LDI for HGI is noticeably smoother, with high values concentrated in transitional zones where topographic and developmental gradients overlap. The emotional dimension presents a "multi-centered, weakly continuous" pattern: while generally low, $IMAX_e$ still exhibits identifiable high-value patches in the Northeast and along the eastern urbanization corridor. Disparities in RT_e and RP_e appear more frequently at urban agglomeration edges, rural-urban interfaces, and around inland nodes, manifesting as scattered hotspots against a weak gradient background. Ultimately, EGI is the smoothest, indicating that peak-like local differences are significantly dampened after aggregation.

These regional variations can be attributed to distinct spatial control mechanisms governing physical versus social processes. Hotspots and gradients in physical metrics are dominated by climatic and topographic contexts: in the arid Northwest and basin environments, low-moisture substrates and strong sensible heat accumulation amplify peak shocks, creating abrupt mutations between neighborhoods. Similarly, the banded disparities in the Southwest basins align with mechanisms where recovery is constrained by ventilation efficiency and heat dissipation difficulties in high-humidity backgrounds, leading recovery times to follow continuous gradients along transition zones. In comparison, inequality on the emotional side is more readily triggered by abrupt shifts within the urban system—specifically in population exposure, development levels, public service accessibility, and social support networks—resulting in discrete "anomaly patches" at urban fringes and rural-urban transitions. Methodologically, the composite indices (HGI, EGI) aggregate shock, cumulative load, and recovery processes, thereby attenuating the peak disparities of single process variables and rendering spatial patterns more continuous. Thus, the dual characteristic of "physical gradients versus social fractures" revealed by the LDI provides direct evidence for tailoring governance priorities and adaptation strategies across different regions.

Note S2: Structural decomposition and component-level analysis of physical and emotional resilience

To dissect the structural underpinnings of HGI and elucidate adaptive mechanisms obscured by aggregate analysis, we decomposed the metric into $IMAX_h$, RT_h, and RP_h, employing multi-dimensional diagnostics across climate zones and spatial mapping (Extended Fig.1; Supplementary Fig. 6-7). Statistical analysis revealed a core resistance-recovery trade-off across environmental gradients. Constrained by inherent humidity barriers and latent heat retention, TSC regions exhibited a typical chronic exposure mode where RT_h was significantly prolonged despite $IMAX_h$ being moderated by maritime influences. Conversely, CTC and PC regions displayed characteristics of acute shock, with resilience deficits stemming primarily from extremely high $IMAX_h$ reflecting a lack of load-handling capacity for episodic heatwaves. Along the urban-rural gradient, megacities leveraged an infrastructure bonus to effectively blunt immediate heat peaks resulting in low $IMAX_h$, yet the immense thermal inertia of high-density built environments incurred a significant heat island penalty causing RT_h to lag far behind rural areas that lacked defense but possessed superior natural ventilation. This mechanistic trade-off projected a distinct pattern of geographical decoupling. $IMAX_h$ followed a pronounced North-High South-Low gradient, with inland basins and arid Northwest regions forming deep red shock-susceptible zones. Mirroring this, RT_h exhibited a South-High North-Low distribution where the Yangtze River Basin and South China coast constituted persistence-susceptible zones due to the dual lock-in effect of high humidity and urban heat islands, while high RP_h bands precisely delineated climate transition zones. Collectively, these findings confirmed that physical resilience was not uniformly distributed but represented a dynamic spatial separation between resistance capacity and recovery efficiency across climatic and urbanization contexts.

The structural decomposition of EGI further confirmed the existence of a prosperity penalty at the micro-mechanistic level, revealing the non-linear breakdown of psychosocial adaptation under extreme climate (Extended Fig.2; Supplementary Fig. 6-8). Unlike the dynamic balance seen in physical resilience, the three components of emotional resilience $IMAX_e$, RT_e, and RP_e exhibited a synchronous double deficit effect across the urban-rural gradient. Megacities not only encountered the highest $IMAX_e$ indicating that negative emotional outbursts among high-density populations were more intense and prone to breaching psychosocial thresholds, but also recorded the longest RT_e. This extended recovery reflected how rapid social metabolism and hyper-competitive environments severely compressed the psychological repair window, causing negative emotions to linger long after heatwaves subsided. Climatic heterogeneity further modulated this response, with TSC regions again emerging as the core of emotional vulnerability. Physiological discomfort driven by humid heat and continuous nocturnal exposure created a potent emotional hysteresis effect, elevating RT_e significantly above arid or cold zones. Spatially, this mechanism projected a characteristic Core-Periphery dual structure. In sharp contrast to the physically robust eastern coastal clusters, dense agglomerations like YRD, PRD, and BTH appeared as extensive low-value emotional heat islands within the EGI map, characterized by high-intensity emotional oscillation or high RP_e and sustained suppression or high RT_e. Conversely, the ecological southwest periphery and less developed small-to-medium cities retained higher emotional elasticity, serving as green sanctuaries for psychological adaptation. This significant spatial mismatch between physical buffering and psychological experience profoundly underscored that technical adaptation alone could not neutralize the psychosocial impact of climate change, suggesting that high-density urban morphology was itself becoming a structural stressor that eroded human emotional resilience.

Note S3: Log-Scale Joint Density Analysis of Resilience–Development Relationships

To quantify the nonlinear links between resilience indicators and development drivers across socio-economic gradients spanning multiple orders of magnitude, this study constructed log-scale joint density plots (Extended Fig.5). The framework combined bivariate kernel density estimation with marginal histograms, and applied base-10 log transforms to the highly skewed population and GDP data to correct their heavy-tailed distributions. This treatment reduced the leverage of extreme outliers from mega-cities on the inferred patterns and, with a nonlinear smoothed regression overlay, robustly revealed the underlying structure of how urban resilience varied with development scale in log space.

The joint-density diagnostics showed that physical and emotional resilience responded to city size in fundamentally different ways. Physical resilience (HGI) exhibited only weak, relatively flat associations with log-transformed population and GDP, with the high-density core concentrated around mid-range values, indicating scale neutrality in physical heat adaptation—large cities did not display a clear per-capita defensive advantage despite resource agglomeration. By contrast, emotional resilience (EGI) showed a pronounced, monotonic negative relationship, with the fitted curve declining steeply as population density and economic mass increased. This pattern pointed to a latent prosperity penalty, or density penalty, in which high-density environments produced by rapid urbanisation concentrated material wealth while materially eroding psychological buffering capacity against climate stress, leaving affluent metropolitan areas as hotspots of emotional vulnerability.

Note S4: Decoupling of resilience patterns revealed by bivariate density plots

Kernel density scatter plots derived from global urban annual means (2020–2024) reveal that HGI and EGI exhibit only a weak negative correlation across the full sample—statistically significant yet negligible in effect size (Extended Fig.10-11). With regression slopes and explanatory power approaching zero, this pattern indicates that these two resilience dimensions do not form a stable linear coupling at the annual scale; rather, their relationship is better characterized by structural decoupling and a multi-modal distribution. The density peak centers on a region where HGI is slightly positive and EGI hovers near zero. Furthermore, quadrant decomposition shows that approximately two-thirds of the city-year units record positive HGI values; notably, a substantial portion of these coincide with negative EGI, suggesting that improvements on the physical side do not necessarily translate into synchronous emotional recovery.

Stratification by climate zone isolates the Arid and Semi-arid regions as having the most pronounced negative correlation, whereas associations in WTC, TSC, and CTC zones remain generally weaker. Structural differences also emerge across quadrants: the CTC zone exhibits the highest proportion of dual-positive outcomes (positive HGI and EGI), whereas WTC regions tend to cluster in the combination of positive HGI but negative EGI. This implies that the climatic background systematically modulates the synchronization—or desynchronization—between physical and emotional resilience.

Further grouping by urbanization level reveals steeper negative slopes in both megacities and rural areas. In megacities specifically, distinct emotional divergence occurs even under conditions of positive HGI, reflecting that high-intensity physical adaptation fails to mitigate psychosocial stress and may instead reinforce adaptive disparities. Conversely, small and medium-sized cities show near-zero or weak positive correlations. Collectively, these findings suggest that the HGI–EGI relationship is co-modulated by climate zones and urbanization processes; thus, it is more accurately interpreted as evidence of stratified decoupling rather than synchronous evolution summarized by a single correlation coefficient.

Note S5: Robustness checks and trend analysis of emotional time series

To diagnose the stability of emotional shifts across varying temporal aggregation scales, we employed the Mann–Kendall test to detect monotonic trends within city-level emotional time series, quantifying their magnitude and direction via Sen's slope estimator (Supplementary Table 1; Supplementary Fig.12). The screening process yielded 1,013 optimal series, all satisfying the 95% significance threshold. With p-values ranging from 0 to 0.0498 (median: 0.0185; interquartile range: 0.0065–0.0328), these results confirm that the observed trends are not artifacts of stochastic fluctuation. Directionally, the trends exhibit a near-equilibrium at the national scale: 513 series (50.6%) show an upward trajectory, while 500 (49.4%) exhibit a decline. This split suggests that emotional evolution is not characterized by a uniform, unidirectional drift across the country. Temporal resolution within the "optimal series" displays a distinct hierarchy, with the 3-hour scale dominating (41.6%), followed by 6-hour (21.1%), 24-hour (20.1%), and 12-hour (17.2%) intervals; consequently, 3-hour emotional data were selected for constructing resilience indices. While the overall magnitude of Sen's slopes is modest, the distribution range broadens significantly with coarser temporal aggregation. Extreme values in 24-hour series reach from −0.0222 to 0.0196, indicating that while temporal smoothing enhances the detection of long-term drifts, it may simultaneously amplify the influence of persistent local deviations on trend estimation.

Despite the balanced dichotomy nationwide, a sharp adaptive divergence emerges within densely populated metropolitan areas. Traditional core cities—typified by Beijing (Sen $\approx -3.3 \times 10^{-5}$), Guangzhou (Sen $\approx -3.4 \times 10^{-4}$), and Chongqing—exhibit a significant erosion of resilience, reflecting the cumulative toll of high-density heat stress and fast-paced social burdens. Conversely, Shenzhen (Sen $\approx +2.7 \times 10^{-4}$) and Shanghai (Sen $\approx +9.0 \times 10^{-5}$) display an encouraging positive trajectory, potentially attributable to superior coastal ventilation or more effective adaptive governance, such as "park city" initiatives. Notably, the most extreme rates of change are confined to peripheral zones. Resource-depleted or arid cities like Shuangyashan (Sen = -0.0223) and Hami (Sen = -0.0094) constitute "vulnerability traps" requiring urgent intervention, highlighting the compound shock of economic contraction and extreme climate exposure on socio-psychological capital. In contrast, high-ecological-function areas such as Ledong (Sen = +0.0197) and Shannan (Sen = +0.0109) serve as "oases" of rapidly improving resilience, leveraging their superior natural baselines. This differentiation underscores that the long-term trajectories of urban emotional resilience are not random walks; rather, they are heavily constrained by path dependencies rooted in urban function, economic transition pathways, and the stock of ecological capital.

Note S6: Indicator considerations for the estimation models employed in this study

To attribute the driving mechanisms underlying urban resilience and its spatial heterogeneity this study developed two categories of non-linear estimation models specifically designed for the Physical Resilience Index (HGI) and the Emotional Resilience Index (EGI). Both modeling frameworks are anchored in a standardized set of explanatory variables capable of robustly characterizing urban structural conditions and morphological variations at a national scale. This comprehensive feature set encompasses socio-economic status represented by Gross Domestic Product (GDP) and Population Count (PopC) topographic context via Elevation (DEM) vegetation and land cover composition including the Normalized Difference Vegetation Index (NDVI) alongside fractional cover indicators for Forest (FT) Barren land (BN) Grassland (GD) Built-up areas (UP) Water bodies (WR) and Cropland (CD) as well as built environment morphology metrics such as Building Height (BH) Building Density (BD) and Floor Area Ratio (FAR) thereby capturing the geographic constraints surface composition and spatial form differences defining distinct urban environments in a unified framework (Supplementary Table 2).

The configuration of these variables adheres to the critical physical pathways governing thermal environment formation. Topography and land surface characteristics constitute the physical baseline where Elevation (DEM) captures the background modulation of thermal lapse rates and local circulation. Regarding surface energy partitioning the Normalized Difference Vegetation Index (NDVI) alongside specific land use categories characterizes variances in canopy structure and evapotranspiration cooling while Water bodies (WR) reflect regulation via high specific heat capacity and Built-up areas (UP) represent impervious substrates characterized by low moisture availability and high heat storage potential. Beyond surface characteristics the three-dimensional morphological structure reshapes the local thermal environment by altering aerodynamic roughness and radiative transfer paths. Grid-average Building Height (BH) and Building Density (BD) signify vertical wind blockage potential and horizontal heat storage surface area respectively while Floor Area Ratio (FAR) serves as a comprehensive metric of development intensity directly associated with longwave radiation trapping efficiency. Finally Population Count (PopC) and Gross Domestic Product (GDP) were employed as critical proxies for anthropogenic heat emissions representing the intensity of metabolic heat release and waste heat discharge associated with high-energy economic activities.

As illustrated by the correlation heatmap (Extended Data Fig. 5), the pairwise Pearson correlation coefficients (r) among the selected independent variables were predominantly low. Specifically, the absolute correlation values ($|r|$) for all variable pairs remained well below the strict threshold of 0.8, signifying a lack of strong linear dependence across the morphological, climatic, and socio-economic predictors. Complementing this diagnostic, the Variance Inflation Factor (VIF) analysis offered a quantitative evaluation of multicollinearity severity. As detailed in Supplementary Table 2, the VIF values for all input features consistently fell beneath the conservative threshold of 5. Collectively, these findings confirm the satisfactory orthogonality of the feature set, validating its suitability for attributing the drivers of urban resilience without significant interference.

Note S7: Cross-regional generalizability and model calibration

We utilized "city-year" observational units from 2020–2024 to validate the model, partitioning the dataset into 80% training and 20% validation subsets. Kernel density scatter plots were generated for 19 distinct city clusters to visualize the agreement between predicted and actual values; in these plots, color gradients represent sample density, while linear regression fits are superimposed on the 1:1 identity line to characterize directional deviation (Extended Fig. 5). Overall, the point clouds adhere closely to the 1:1 line with high-density regions clustering along the diagonal, indicating robust model calibration across the full value spectrum. Validation metrics for the full sample (N=619,996) yield an R^2 of 0.95, a mean absolute error (MAE) of 0.014, and a bias of −0.002, reflecting minimal error magnitudes and negligible systematic bias. Importantly, these performance patterns remain consistent across disaggregated city clusters, demonstrating that LightGBM maintains stable generalizability in cross-regional contexts. This consistency underscores the algorithm's capacity to precisely capture the localized emotional baselines and fluctuation dynamics intrinsic to diverse geographical units.

Note S8: Attribution of driving mechanisms for Best Lag (BL)

SHAP-based attribution analysis identified heat hazard characteristics as the predominant drivers determining the Best Lag (BL) for public emotional response, significantly outweighing other explanatory categories (Supplementary Fig. 15). Specifically, GDP made the largest contribution at 16.52%, followed sequentially by RP_h (13.11%), BL (12.86%), $IMAX_h$ (12.08%), and RT_h (11.93%). In contrast, topographic and ecological contexts represented by DEM (7.33%) and NDVI (5.19%) provided secondary yet stable boundary constraints, while land cover and morphological variables generally functioned as subtle regulators of local microclimatic conditions.

Dependence analysis further elucidated the distinct operational modes of these key factors. GDP exhibited a robust non-linear attenuation pattern where its influence on the lag structure diminished rapidly within lower GDP ranges and plateaued at higher levels, indicating a diminishing marginal effect of economic capacity on optimizing lag configuration. Conversely, RP_h displayed a fluctuating response characterized by multiple inflection points, suggesting that cumulative heat load altered the lag window by triggering distinct recovery states rather than through monotonic accumulation. Notably, the positive contribution of $IMAX_h$ intensified significantly within the extreme high-temperature range, implying that once peak heat shock surpassed a critical threshold, it fundamentally reshaped the optimal lag structure.

Note S9: Temporal trajectories and component-level drivers of physical and emotional resilience (2025–2100)

Time series reconstructions derived from an ensemble of 13 CMIP6 models indicated that under three SSP pathways, both HGI and EGI evolved with a distinct non-linear morphology characterized by moderate mid-term changes followed by accelerated late-term shifts (Extended Fig.7-9; Supplementary Fig.16-17). However, a temporal mismatch existed in their sensitivity to emission intensities. EGI exhibited quasi-plateau characteristics between 2025 and 2050, where the SSP1-2.6 scenario registered a slight uptake of approximately 0.1% and SSP5-8.5 remained largely static with a marginal decline of 0.1%. It was only after 2050 that a deep downward trajectory initiated, resulting in declines of 7.8%, 17.1%, and 20.3% relative to the baseline by the end of the century. In contrast, the attenuation of HGI displayed a marked early onset. Cumulative declines of 3.1% to 4.8% emerged within the first half of the century, accelerating further in the latter half as high-emission pathways locked in; by 2100, reductions reached 13.9%, 16.1%, and 25.4% relative to 2025. These scenario-dependent trajectories suggested that high-emission pathways not only significantly amplified the magnitude of long-term decay but also widened the uncertainty bandwidth of predictions. Consequently, the structure of systemic risk diverged drastically in the second half of the century driven by scenario disparities.

The evolution of six structural components further elucidated the micro-dynamic sources of this index attenuation. Across all scenarios, the sustained rise in $IMAX_h$,

RT_h, and RP_h confirmed a synchronous deterioration in physical heat shock intensity, recovery lag, and process volatility, while the parallel elevation of $IMAX_e$, RT_e, and RP_e signaled a systemic amplification of negative emotional peaks and hysteresis effects. This deteriorating trend presented a clear gradient differentiation across scenarios, driven primarily by incremental changes post-2050. Under SSP5-8.5, the magnitude of deterioration for physical and emotional components reached its zenith: $IMAX_h$ and RT_h surged by 35.9% and 50.1% respectively, while $IMAX_e$ and RT_e rose by 25.6% and 46.4%, far exceeding the moderate increases observed under SSP1-2.6. Notably, among all components, RT_h and RT_e exhibited the highest scenario sensitivity. This revealed that structural degradation at the recovery end, rather than mere peak elevation, constituted the dominant channel driving resilience collapse in a high-emission future. Furthermore, the physical and emotional linkages displayed stronger synergistic amplification characteristics in the latter half of the century.

C. Supplementary Tables

Supplementary Table 1. *Statistical significance and magnitude of emotional trends in 40 representative cities: Z-values, P-values, Sen's slopes and Best lag days derived from 3-hour scale observations.*

City	Z Value	P Value	Sen Slope	Best Lag days
Beijing	-2.3683	0.0179	-0.000023	3.6
Shanghai	7.8170	5.33e-15	0.000078	2.9
Guangzhou	-4.0572	0.00005	-0.000059	2.5
Shenzhen	2.3623	0.0182	0.000028	2.9
Tianjin	3.0763	0.0021	0.000054	3.8
Chongqing	-1.9819	0.0475	-0.000037	3.4
Nanjing	3.8714	0.0001	0.000025	2.6
Suzhou	9.5870	0.0000	0.000146	3.0
Hangzhou	-2.7953	0.0052	-0.000041	2.6
Wuhan	-2.3090	0.0209	-0.000032	3.0
Xian	-2.0535	0.0400	-0.000035	3.2
Wuxi	-4.4134	0.00001	-0.000073	2.9
Ningbo	-5.6040	2.09e-08	-0.000114	2.9
Changsha	-6.0617	1.35e-09	-0.000033	2.8
Hefei	-6.8170	9.30e-12	-0.000183	3.4
Fuzhou	3.0925	0.0020	0.000086	2.4
Jinan	-2.3610	0.0182	-0.000054	3.5
Shenyang	2.3145	0.0206	0.000044	3.3

Haerbin	2.0689	0.0386	0.000019	2.9
Dalian	-4.8353	1.33e-06	-0.000072	3.3
Xiamen	-3.2981	0.0010	-0.000042	2.2
Foshan	2.3862	0.0170	0.000023	2.8
Nanning	-2.5295	0.0114	-0.000054	2.0
Haikou	2.5018	0.0124	0.000115	2.2
Guiyang	2.6206	0.0088	0.000032	2.6
Lanzhou	-2.7202	0.0065	-0.000124	3.3
Nanchang	-2.7852	0.0053	-0.000040	3.2
Huhehaote	-3.7197	0.0002	-0.000084	3.2
Wulumuqi	2.3429	0.0191	0.000055	3.6
Changzhou	-8.4626	0.0000	-0.000326	3.3
Dongguan	3.5582	0.0004	0.000072	3.1
Huizhou	-2.9159	0.0035	-0.000088	2.5
Jiaxing	-2.3576	0.0184	-0.000031	2.8
Nantong	-2.5822	0.0098	-0.000045	2.2
Quanzhou	-4.8088	1.52e-06	-0.000094	2.3
Wenzhou	-2.0244	0.0429	-0.000042	2.2
Xuzhou	3.4753	0.0005	0.000111	3.4
Yantai	2.0603	0.0394	0.000037	2.9
Zhongshan	2.2163	0.0267	0.000070	2.3

Supplementary Table 2. *Summary of explanatory variables, physical mechanisms, and variance inflation factors (VIF)*

Category	**Variable**	**Abbreviation**	**Physical Mechanism & Rationale**	**VIF**
Physical Resilience Metrics	Heat Recovery Time	RT_h	Duration required for the thermal environment to return to baseline levels	1.11
	Peak Heat Severity	$IMAX_h$	Maximum intensity of the heatwave event relative to the baseline	1.40
	Cumulative Heat Magnitude	RP_h	Total accumulated thermal stress (area under the curve) during the event	1.33
Emotional Resilience Metrics	Emotion Recovery Time	RT_e	Duration for public sentiment to recover to baseline levels after heat	1.11
	Peak Emotional Severity	$IMAX_e$	Maximum intensity of negative emotional expression during the heatwave	1.16
	Cumulative Emotional Perturbation	RP_e	Total accumulated emotional stress load during the event	1.19
Socio-economic Status	Gross Domestic Product	GDP	Proxy for anthropogenic waste heat discharge from economic activities	2.94
	Population Count	PopC	Represents metabolic heat release and human activity intensity	3.26
Topographic Context	Elevation	DEM	Background modulation of thermal lapse rates and local circulation	2.32
Vegetation & Land Cover	Normalized Difference Vegetation Index	NDVI	Characterizes vegetation vitality and surface energy partitioning	4.76
	Forest / Grassland / Cropland	FT / GD / CD	Capture canopy structures and evapotranspiration cooling capacities	4.88 / 4.27 / 4.94
	Water Bodies	WR	Reflects thermal regulation via high specific heat capacity	1.34
	Barren Land / Built-up Areas	BN / UP	Impervious substrates with low moisture and high heat storage	4.17 / 4.60
Built Environment	Grid-average Building Height	BH	Signifies vertical wind blockage potential and aerodynamic	4.75
	Grid-average Building Density	BD	Horizontal surface area available for solar heat storage	4.55
	Floor Area Ratio	FAR	Metric of development intensity	4.42

Supplementary Table 3. *The CMIP6 models used in the analysis. Listed are the ensemble size of the ALLforcing, NAT-forcing, GHG-forcing, segments of piControl simulations, SSP1-2.6, SSP2-4.5, andSSP5-8.5 experiments, and the equilibrium climate sensitivity (ECS) of climate models. The ECS estimatesare from Zelinka et al.(2020)*

MODEL	ALL	NAT	GHG	piControl	SSP1-2.6	SSP2-4.5	SSP5-8.5	ECS (K)
ACCESS-CM2	3	3	3	1	3	3	3	4.72
ACCESS-ESM1-5	3	3	3	1	3	3	3	3.88
BCC-CSM2-MR	3	3	3	1	1	1	1	3.02
CanESM5	10	10	10	1	25	25	25	5.64
CESM2	3	3	3	1	3	3	3	5.15
CNRM-CM6-1	6	6	6	1	6	6	6	4.83
FGOALS-g3	3	3	3	1	1	1	1	2.87
GFDL-ESM4	3	3	3	1	1	1	1	2.65
GISS-E2-1-G	5	5	5	1	5	5	5	2.72
IPSL-CM6A-LR	6	6	6	1	6	6	6	4.56
MIROC6	3	3	3	1	3	3	3	2.60
MRI-ESM2-0	3	3	3	1	1	1	1	3.15
NorESM2-LM	3	3	3	1	1	1	1	2.54
SUM (runs)	54	54	54	13	59	59	59	—

D. Supplementary Figures

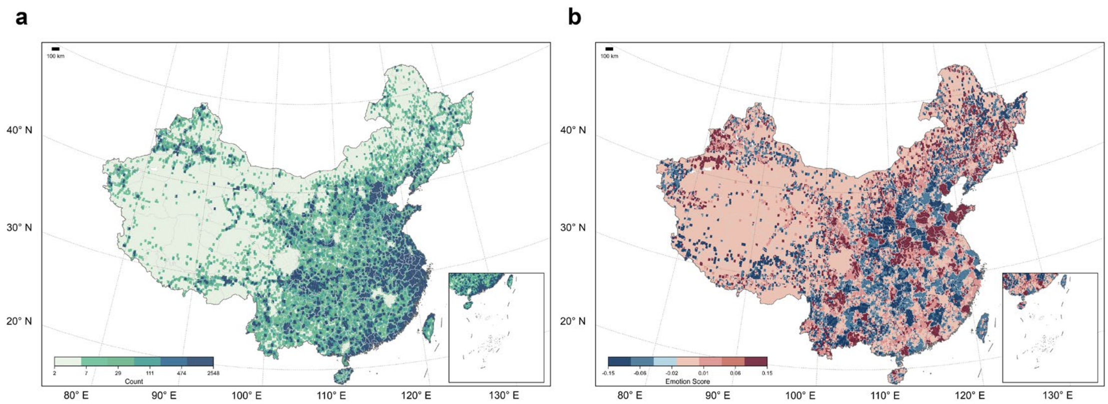

Supplementary Fig. 1. Spatial coverage of social emotion data.a, Density of geolocated Weibo comments used in the analysis. b, Spatial distribution of calculated sentiment scores.

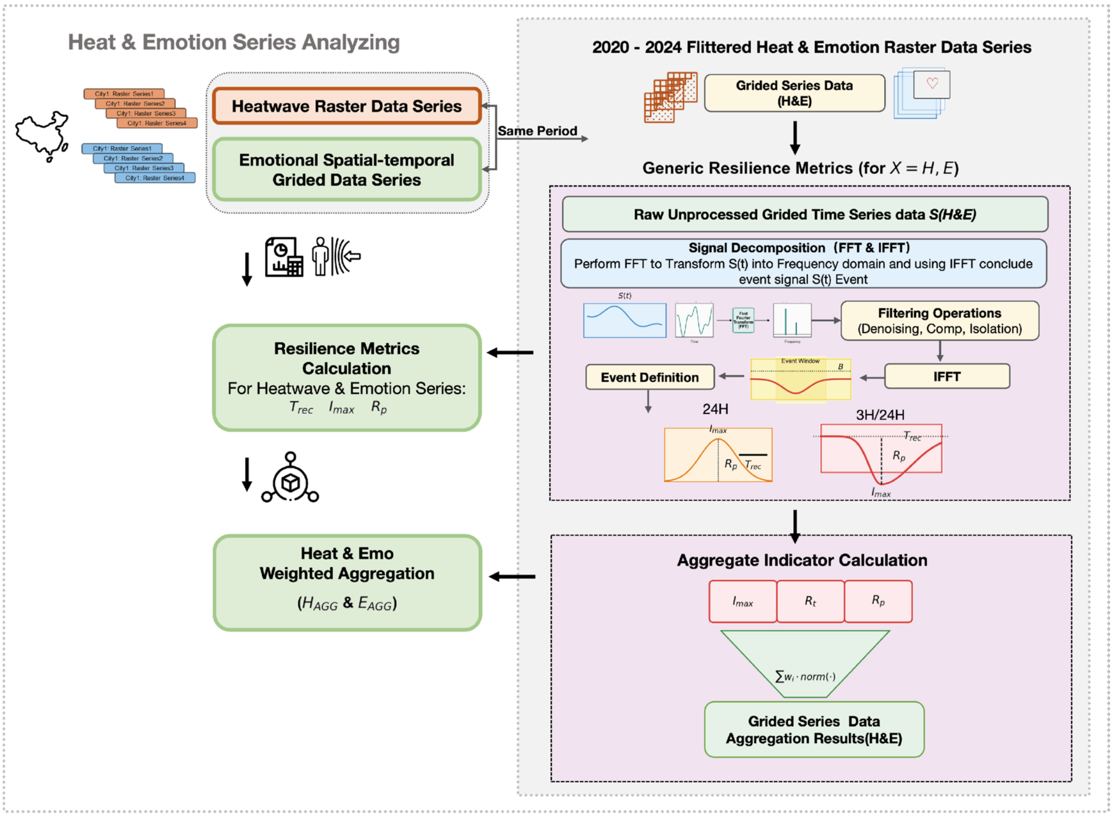

Supplementary Fig. 2. Computational framework for quantifying heat and emotional resilience metrics.

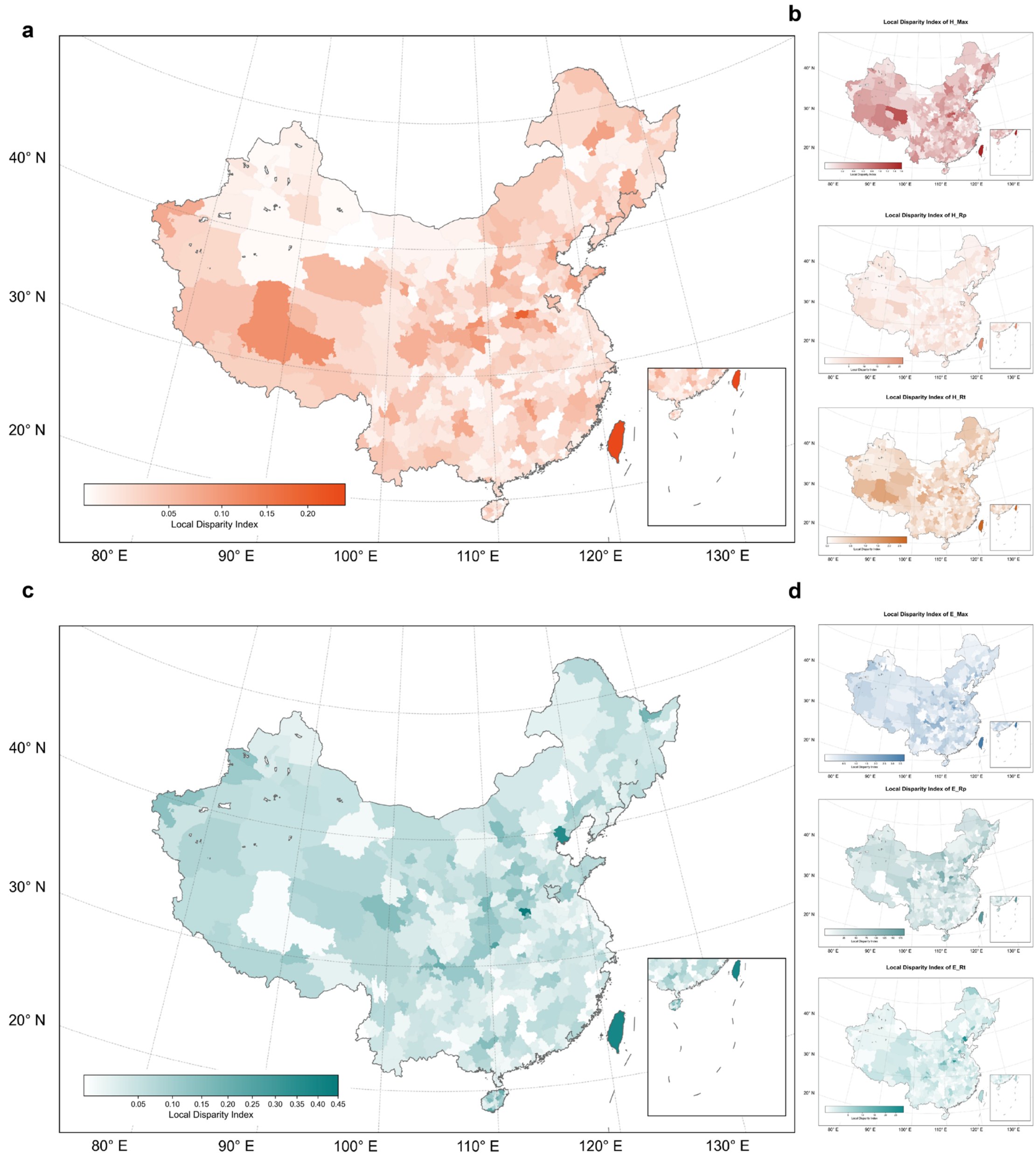

Supplementary Fig. 3. Spatial patterns of local inequality characterized by the Local Disparity Index (LDI). a, c, HGI (a) and EGI (c). b, Heat components ($IMAX_h$; RP_h, and RT_h). d, Emotion components ($IMAX_e$; RP_e, and RT_e). Darker shades indicate higher disparity.

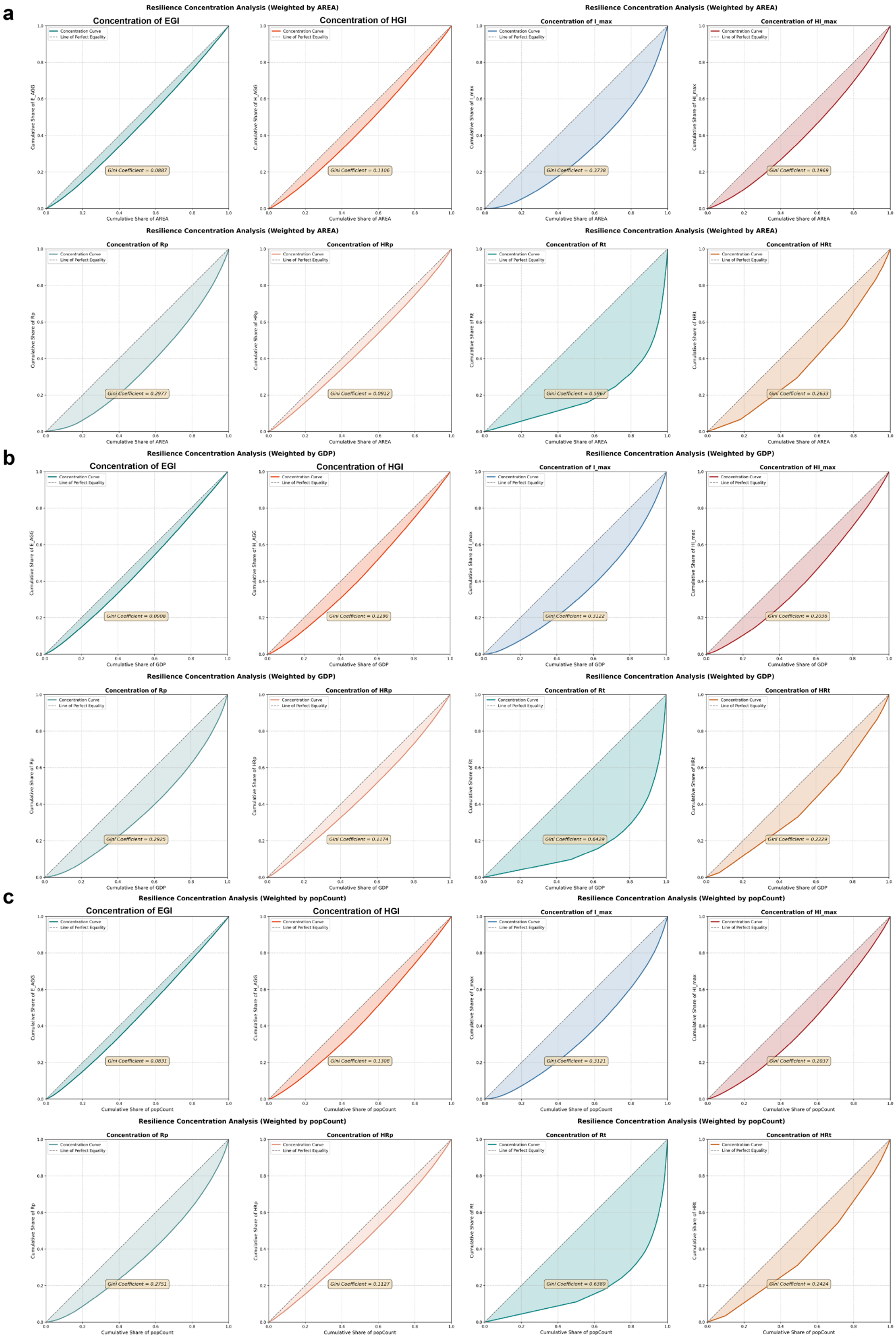

Supplementary Fig.4. Lorenz curves quantifying inequality in resilience metrics. a, Population-weighted; b, GDP-weighted; and c, Area-weighted. The diagonal line represents perfect equality.

Supplementary Fig. 5. Geographical distribution of the 19 urban agglomerations.

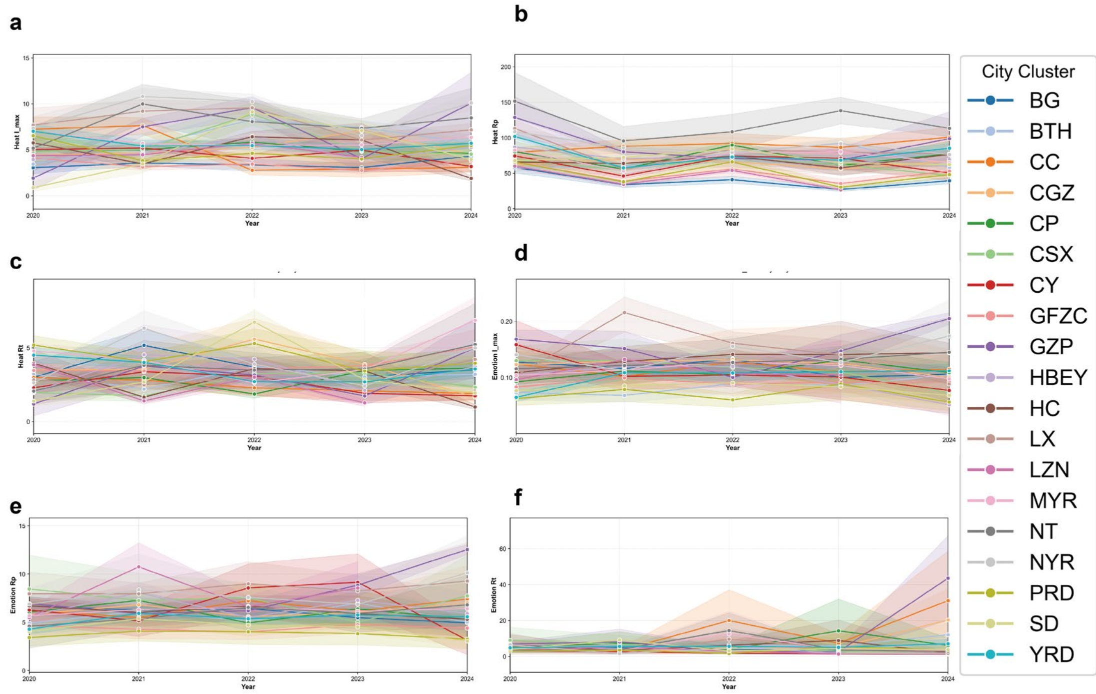

Supplementary Fig. 6. Interannual variability of resilience components across city clusters (2020 – 2024). a – c, Heat components: $IMAX_h$ (a), RP_h and RT_h (c). d – f, Emotion components: $IMAX_e$(d), RP_e *(e)*, and RT_e (f). Coloured lines represent individual city clusters; shaded areas denote 95% confidence intervals.

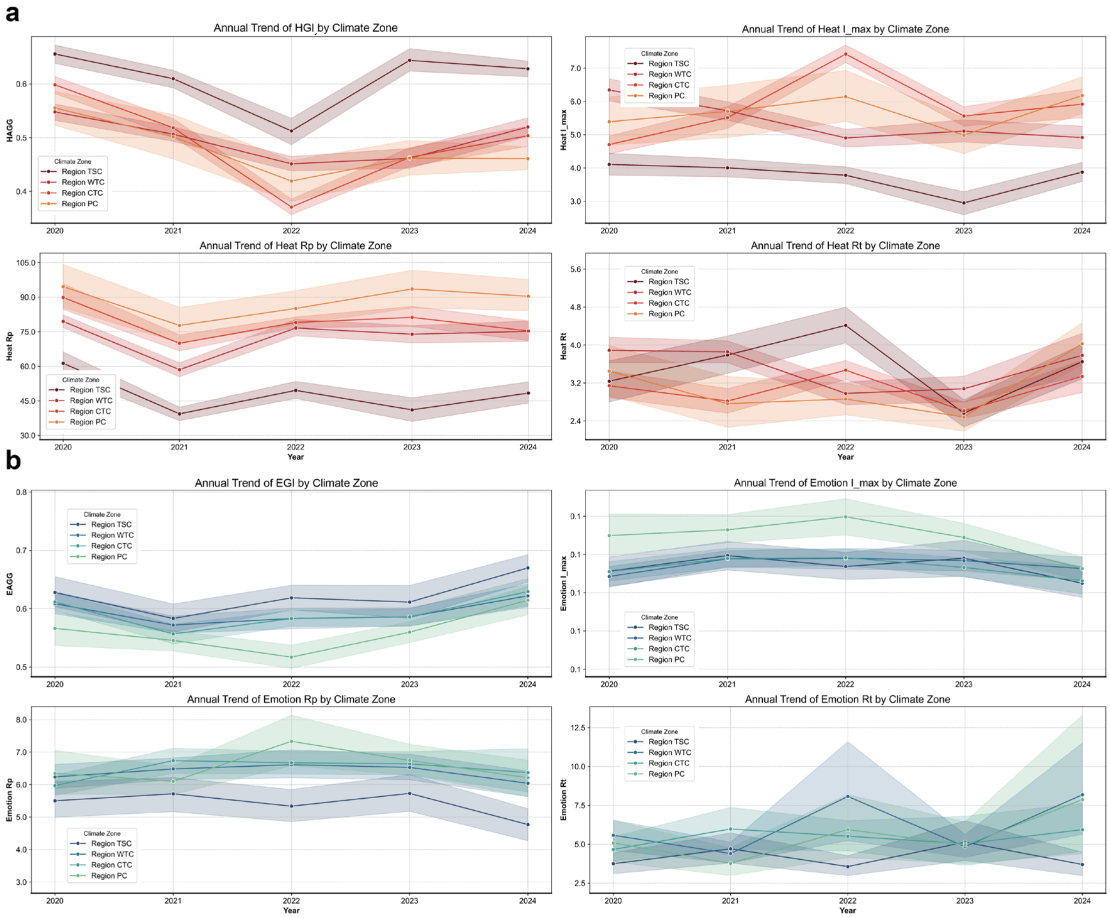

Supplementary Fig. 7. Interannual variability of resilience metrics across climate zones (2020 – 2024). a, Heat metrics: HGI, $IMAX_h$; RP_h, and RT_h. b, Emotion metrics: EGI, $IMAX_e$; RP_e, and RT_e. Coloured lines represent climatic regions (TSC, WTC, CTC, PC); shaded areas denote 95% confidence intervals.

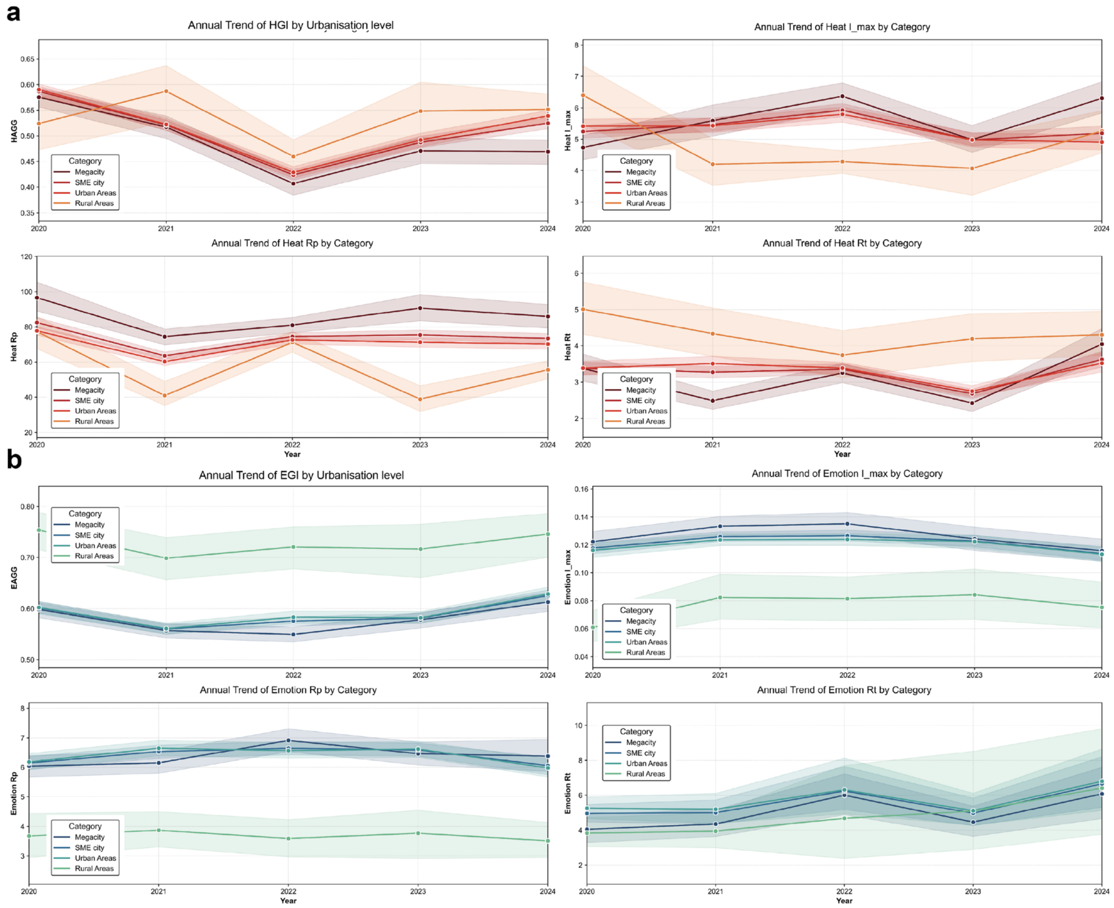

Supplementary Fig. 8. Interannual variability of resilience metrics across urbanization levels (2020 – 2024). a, Heat metrics: HGI, $IMAX_h$; RP_h, and RT_h. b, Emotion metrics: EGI, $IMAX_e$; RP_e, and RT_e. Coloured lines represent urbanization categories (Megacity, SME City, Urban Areas, Rural Areas); shaded areas denote 95% confidence intervals.

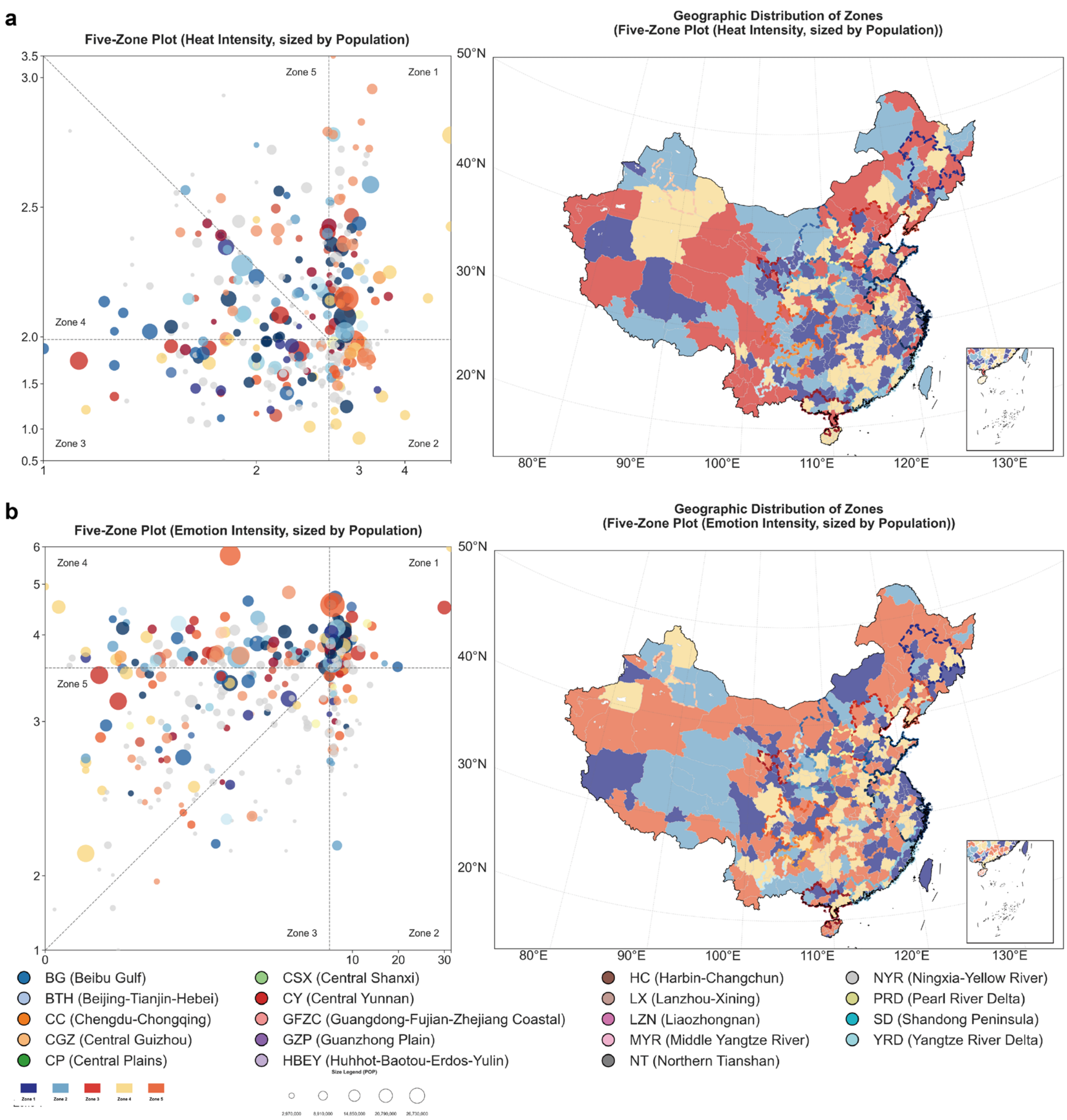

Supplementary Fig. 9. Pentagonal scatter plots mapping 357 cities based on population weighting. a, b, Classification of Heat Intensity (a) and Emotion Intensity (b). Bubble sizes indicate population magnitude, while colours represent the 19 city clusters.

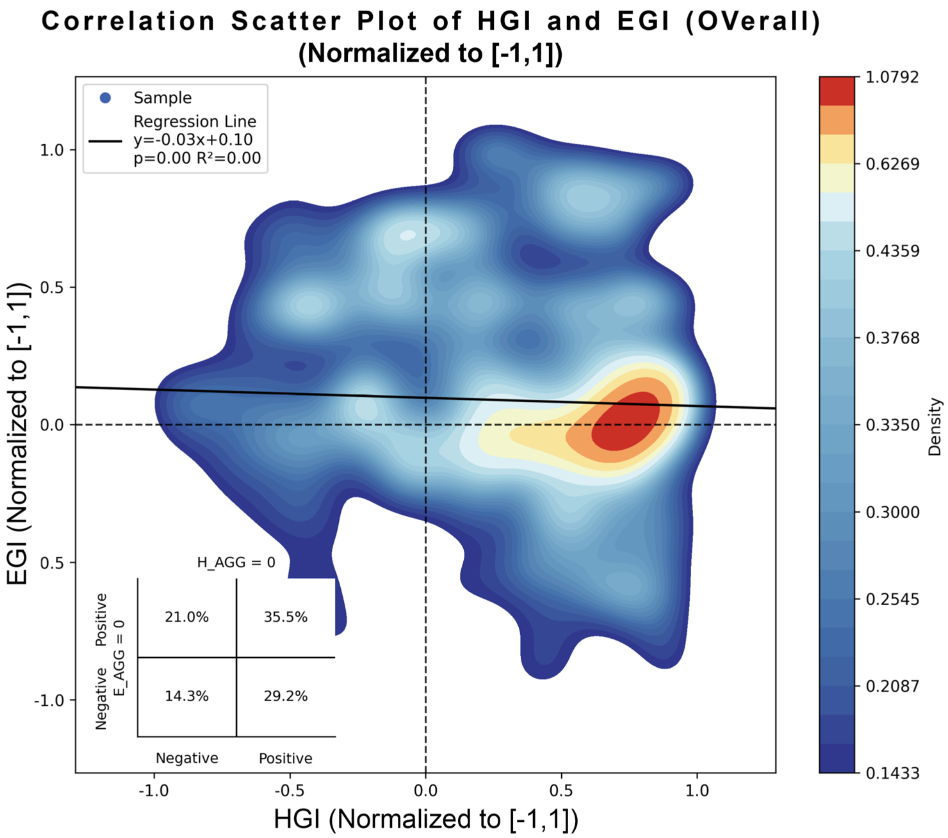

Supplementary Fig.10. Bivariate KDE analysis of HGI and EGI decoupling.

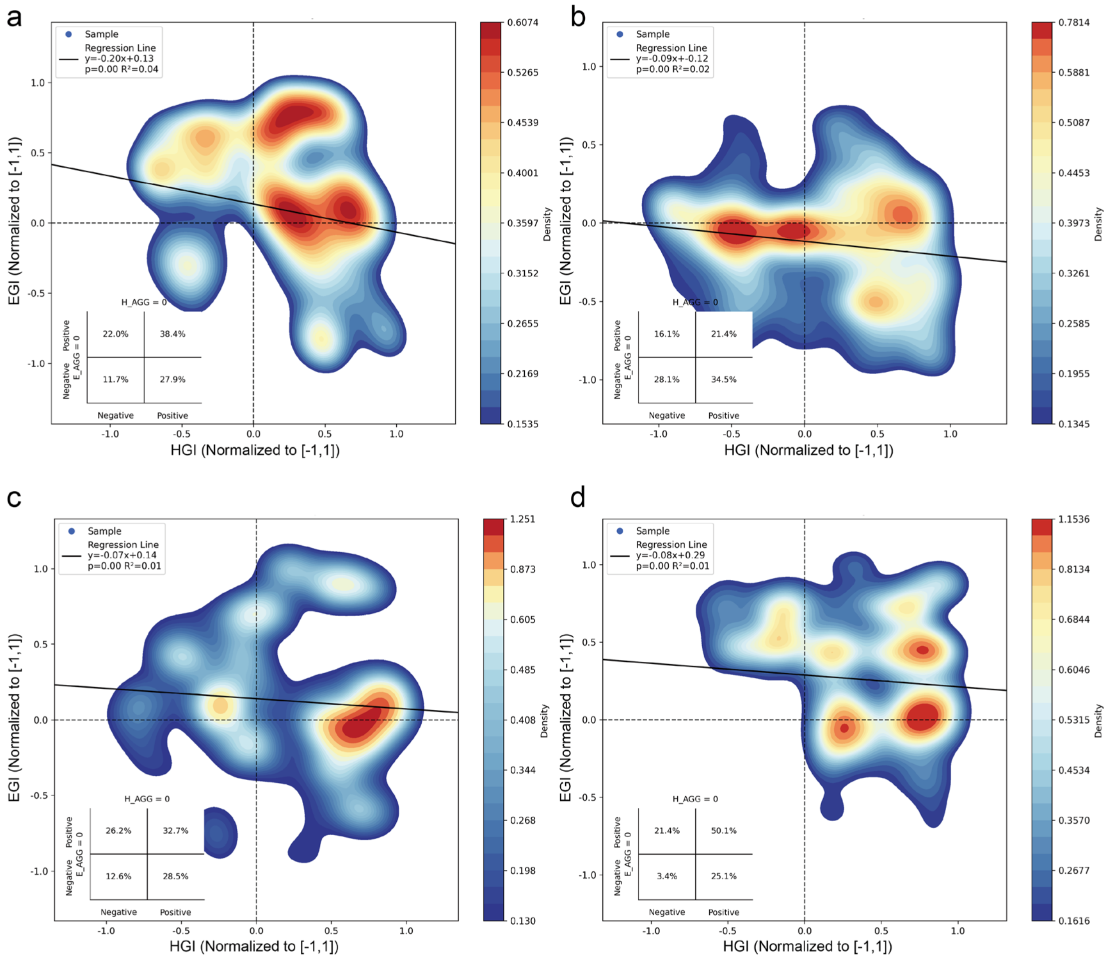

Supplementary Fig.11. Bivariate KDE analysis of HGI and EGI decoupling across climatic zones. a, Climatic regions: tropical－subtropical (TSC); b, warm temperate (WTC); c, cold temperate (CTC); d, plateau climate (PC).

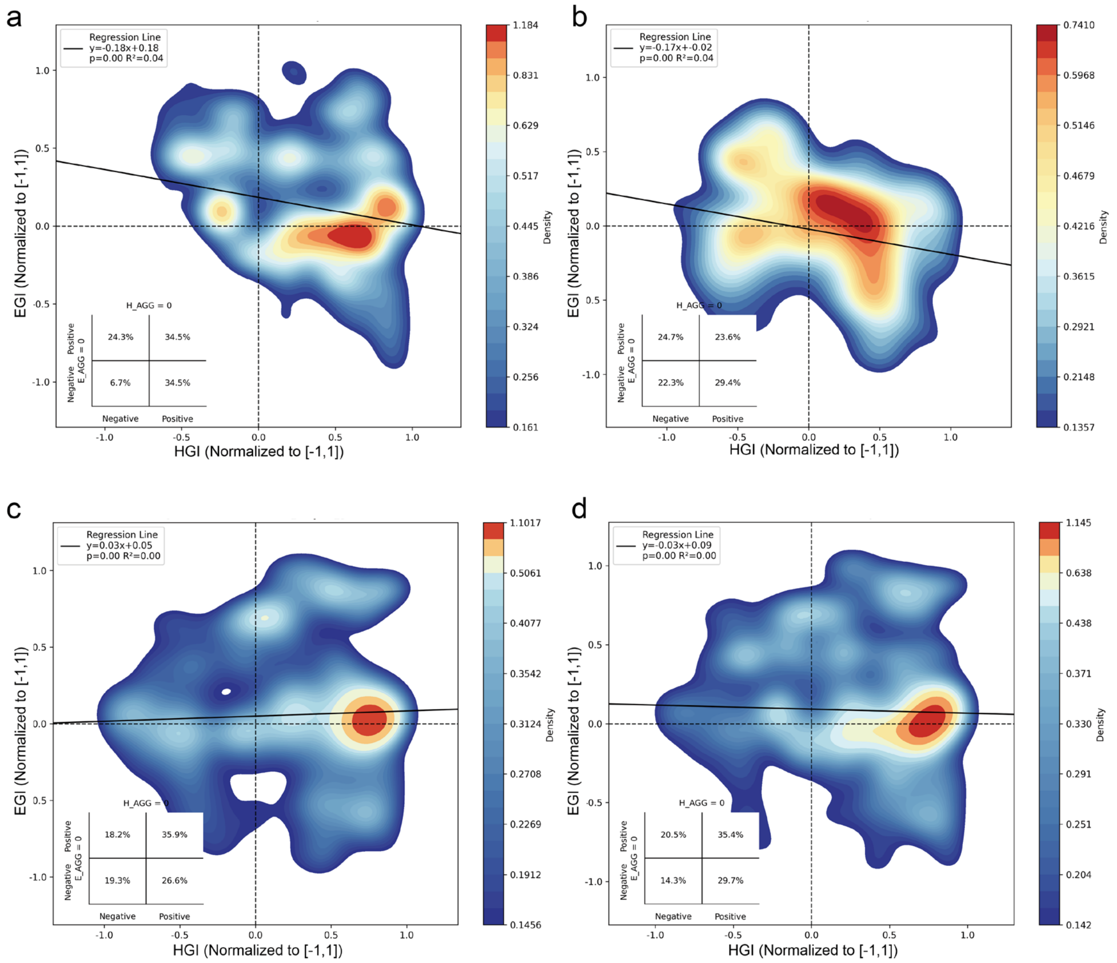

Supplementary Fig.12. Bivariate KDE analysis of HGI and EGI decoupling across city scale and urban contexts. a, megacity; b, SME City; c, urban areas; d, rural areas.

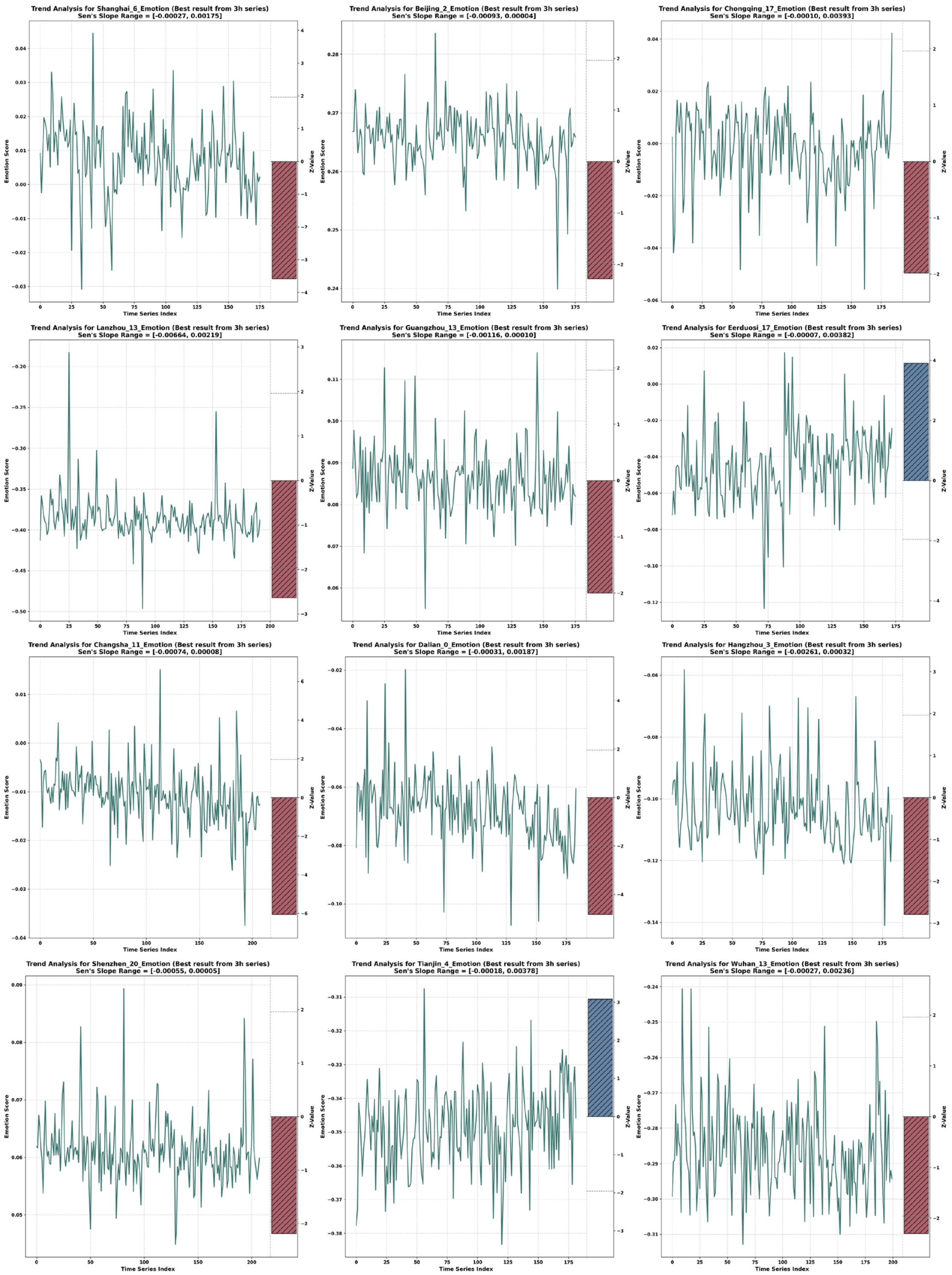

Supplementary Fig.13. Mann－Kendall trend detection and Sen’s slope quantification for twelve representative cities. Bars are colour-coded to indicate the trend direction: red represents a positive Sen’s slope (associated with active recovery or increasing resilience), whereas blue represents a negative Sen’s slope (indicating persistent stress accumulation or decreasing resilience). The asterisk (*) denotes statistical significance at the 0.05 level.

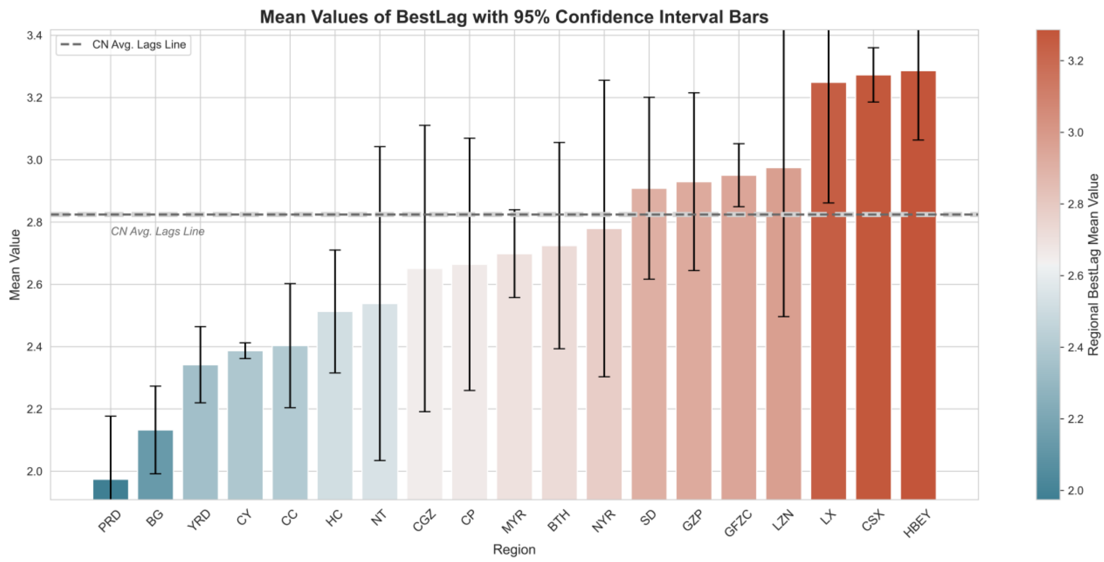

Supplementary Fig.14. Regional heterogeneity in the lag response of emotional sentiment across 19 major urban agglomerations. The bar chart displays the estimated Best Lag (BL) days for each city cluster, derived from Distributed Lag Non-linear Models (DLNM). The height of each bar represents the regional mean, while error bars denote the 95% confidence intervals (95% CI).

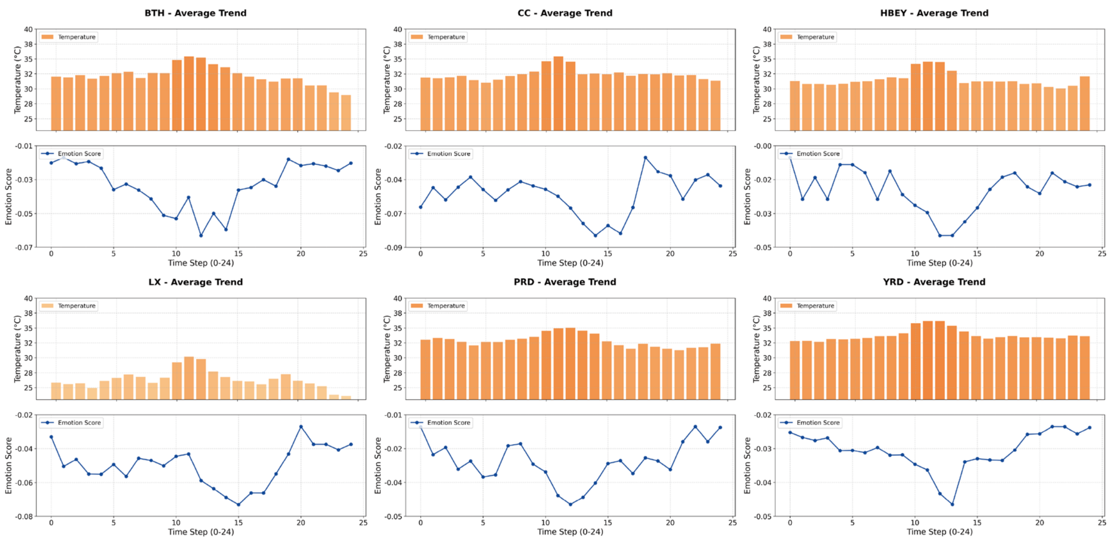

Supplementary Fig.15. Daily time series of maximum temperature and emotion scores across six representative urban agglomerations.

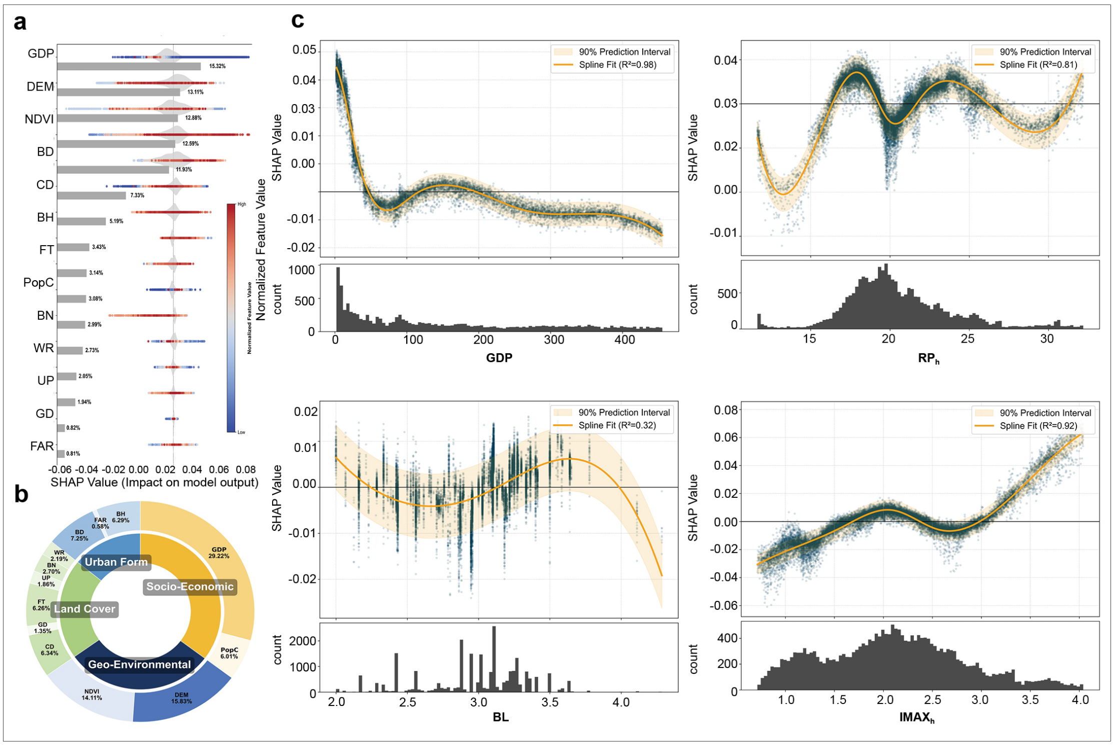

Supplementary Fig.16. Global importance and local effect of each feature in the ensemble learning models for BL.

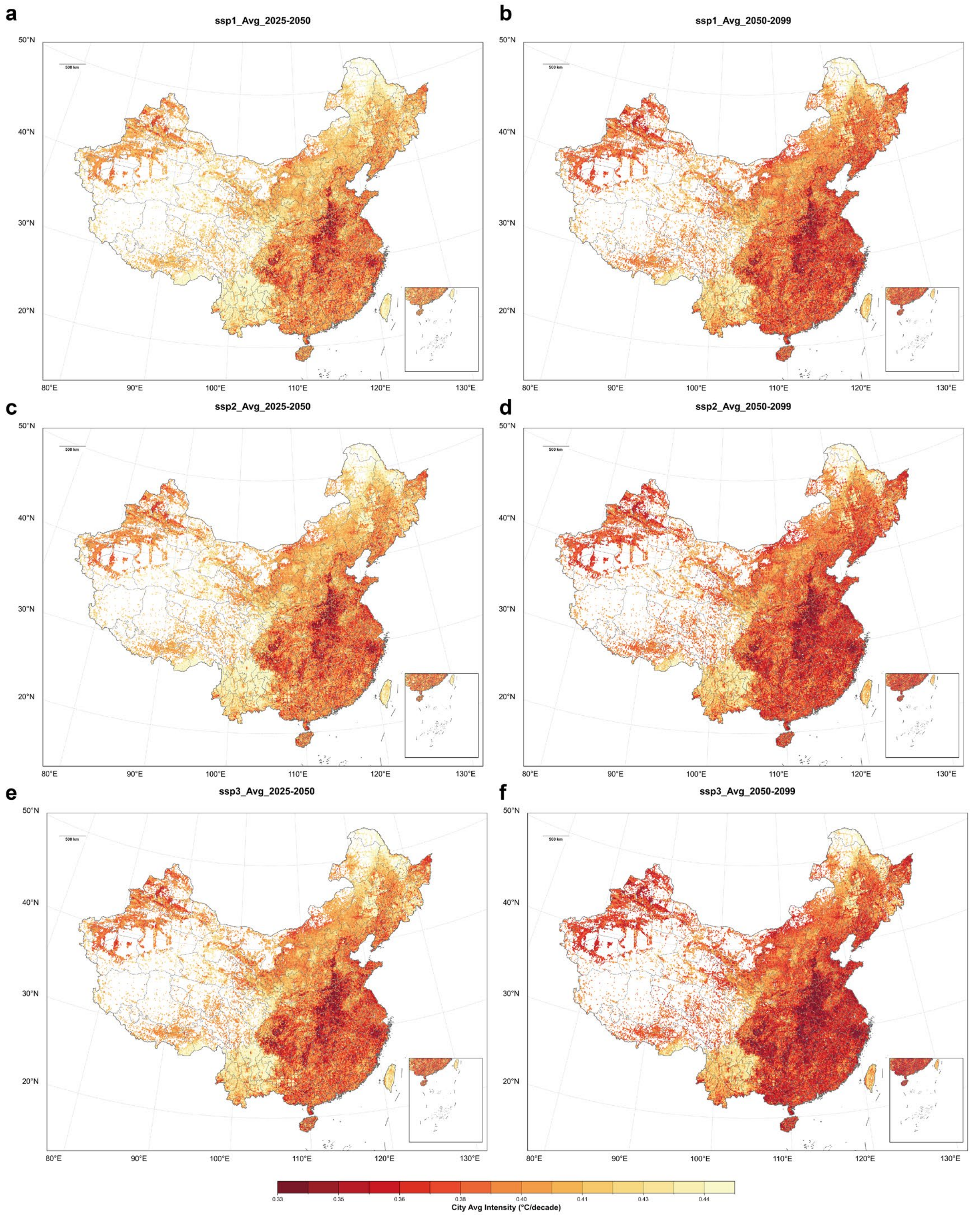

Supplementary Fig.17. Projected spatiotemporal evolution of HGI under different SSP–RCP scenarios. The maps visualize the projected mean HGI across Chinese cities for the near-term (2025–2050) and long-term (2050–2100) periods. a, b, Spatial distribution of mean HGI under the SSP1-2.6 scenario for 2025–2050 (a) and 2050–2100 (b). c, d, Projections under the SSP2-4.5 scenario for the same time periods. e, f, Projections under the SSP5-8.5 scenario.

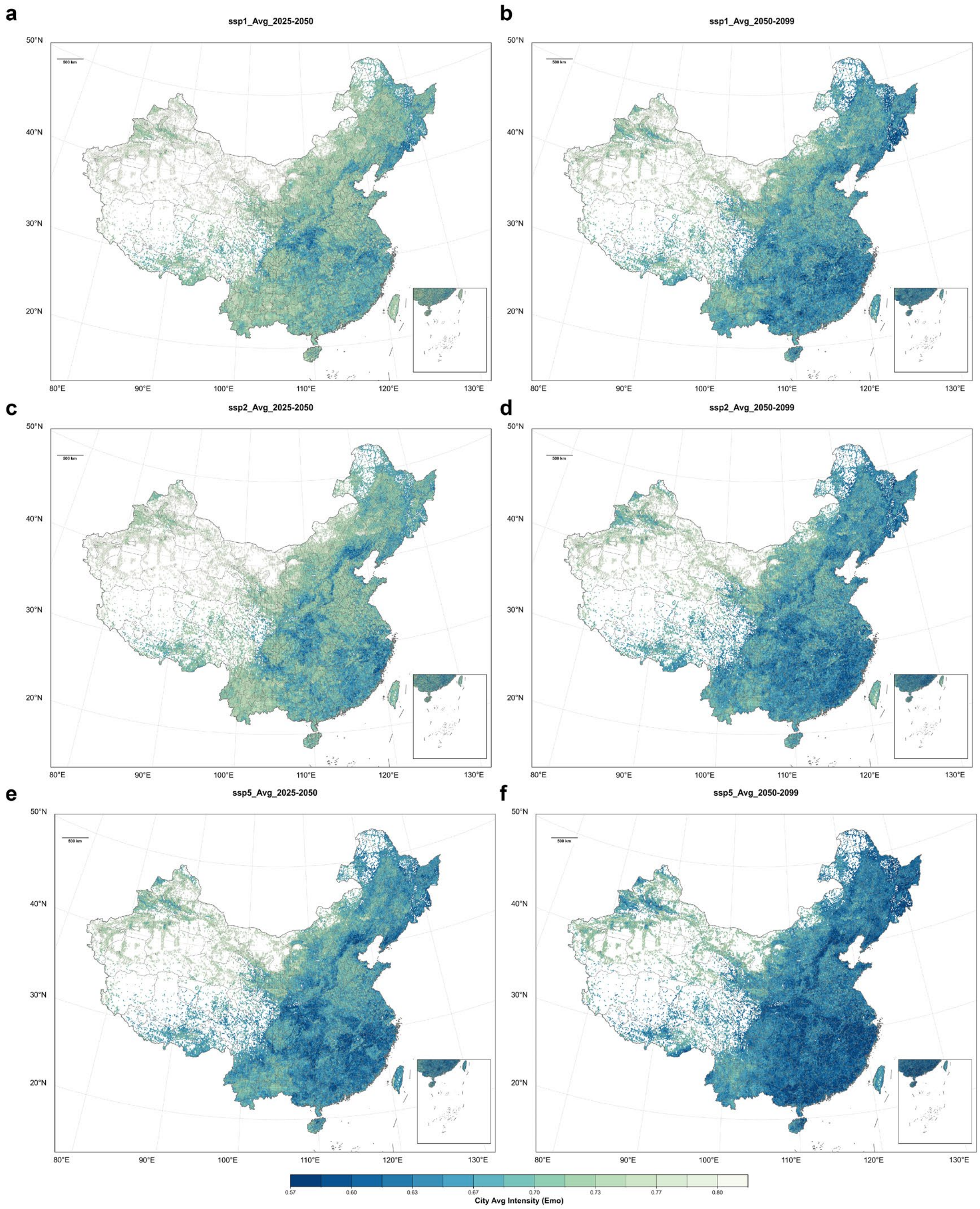

Supplementary Fig.18. Projected spatiotemporal evolution of EGI under different SSP–RCP scenarios. The maps visualize the projected mean EGI across Chinese cities for the near-term (2025–2050) and long-term (2050–2100) periods. a, b, Spatial distribution of mean EGI under the SSP1-2.6 scenario for 2025–2050 (a) and 2050–2100 (b). c, d, Projections under the SSP2-4.5 scenario for the same time periods. e, f, Projections under the SSP5-8.5 scenario.

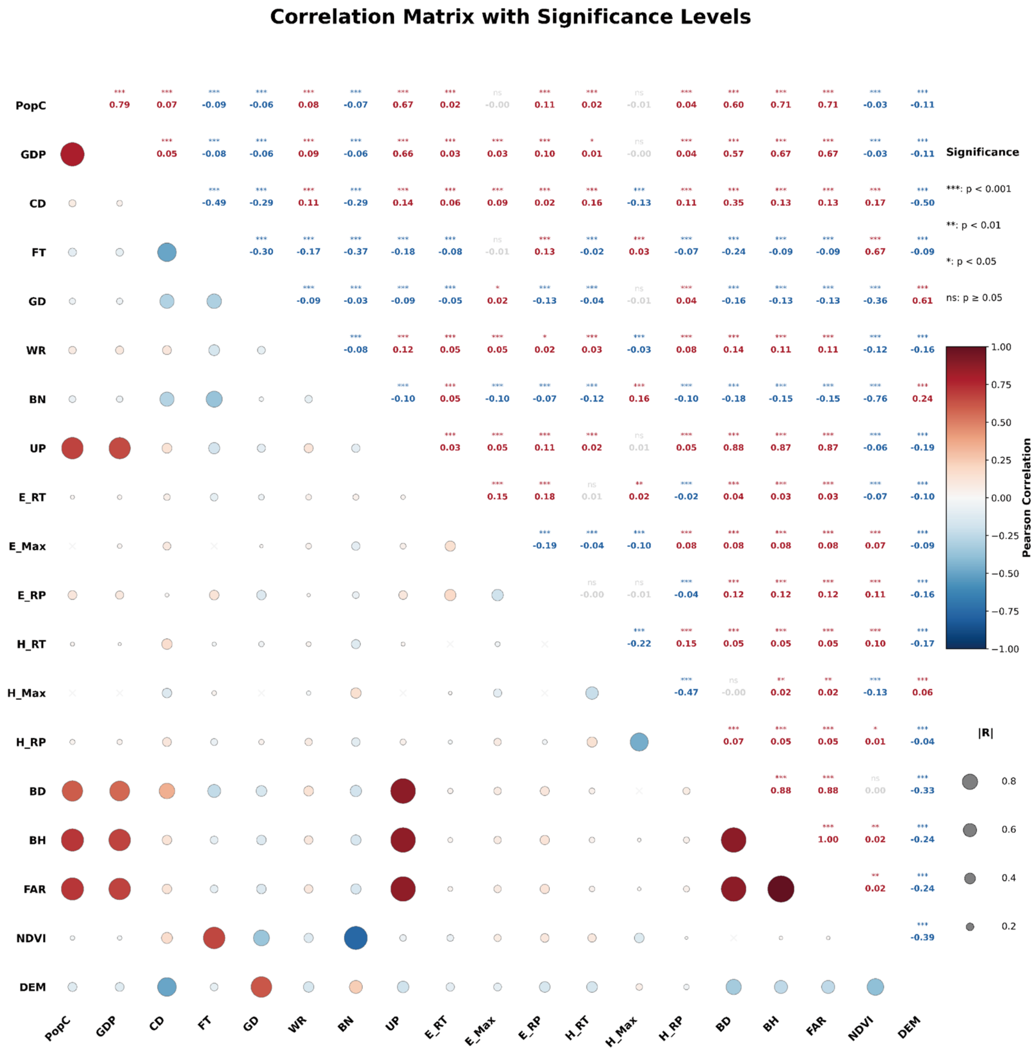

Supplementary Fig.19. Pearson correlation matrix of urban drivers and resilience metrics.